

Techniques.



Non-Intrusive Multi-Fidelity Reduced Order Modeling

using Adaptive Sparse Grids.

by

S.M.C. Bohnenn

to obtain the degree of Master of Science in Applied Physics at the Delft University of Technology, to be defended publicly on March 3rd, 2023 at 13:00 hour.

Student number: 5407540

Project duration: March, 2022 – March, 2023

Thesis committee: Dr. Z. Perkó, TU Delft, supervisor

Dr.ir. D. Lathouwers, TU Delft, supervisor

Prof.dr.ir. M.B van Gijzen, TU Delft

An electronic version of this thesis is available at http://repository.tudelft.nl/.



Acknowledgements

I'd like to thank everyone who has contributed to my Master's thesis project. Firstly, I'd like to extend my appreciation to Zoltan for his guidance and insights throughout the project. You not only provided me with the essential insights that I needed to move forward in my project, but also kept faith in both me and the project even when I was feeling lost. I enjoyed our meetings, they felt more like brainstorming sessions where we worked together to solve the problem. You emphasized the importance of good teachers, and in my opinion, you are among that category. Secondly, I would like to thank Danny for his expertise and insights, particularly during the project's second half. Your guidance and our meetings helped me to stay focused and think critically throughout my project.

I want to thank my friends and family for their unlimited support. I want to thank my parents for believing in me and sending their support all the way from the Achterhoek. I want to thank my friends, of whom most do not have a technical background, for listening to me talking about MATLAB debugging, neutrons flying around in nuclear reactors, and occupied high-performance computers. I want to express my gratitude to everyone at the RID for making me feel at home in the group. Emma, Ruben, and Thomas, thank you for the many fun ping pong games, chocolate treats, walks around campus, and coffee breaks. To my housemates in Rotterdam, thank you for motivating me to give my best every day, providing the best distractions, and supporting me throughout. Lastly, I want to thank Luc for always having faith in me, being there for me during setbacks, and celebrating every milestone with me.

S.M.C. Bohnenn Delft, February 2023

Abstract

Computational power is a challenge when it comes to the high-fidelity modeling of nuclear reactors. Detailed simulations of reactor physics involve complex calculations that require significant computing resources, which can be time-consuming and expensive. Reduced Order Modeling (ROM) allows for an approximation of a complex model by only capturing the essential features, thereby reducing the computational load. A reduced order model provides computationally efficient approximations of a system, but it requires still many evaluations of a high-fidelity model to capture all the dynamics. Using the adaptive sparse grid can reduce the number of evaluations needed, though the construction of the reduced order model is still computationally intensive.

The aim is to minimize the computational workload involved in constructing a reduced-order model during the offline phase. This is achieved by decreasing the number of high-fidelity model evaluations necessary for building the reduced order model while maintaining accurate results. To this end, the existing adaptive proper orthogonal decomposition algorithm is enhanced by employing multi-fidelity techniques. Multi-fidelity methods aim to combine large amount of low-fidelity data with a limited amount of high-fidelity data to compute accurate, yet computationally inexpensive approximations. Two novel multi-fidelity reduced order model methods based on proper orthogonal decomposition are proposed; Filtered Bi-Fidelity Adaptive Proper Orthogonal Decomposition (FB-POD) algorithm and Adapted Bi-Fidelity Proper Orthogonal Decomposition (AB-POD). These models are evaluated on two different test cases, and the balance between the accuracy of each multi-fidelity ROM and the computational cost, measured by the number of high-fidelity evaluations, is investigated. In specific cases, the proposed methods significantly reduce the number of high-fidelity evaluations compared to the single high-fidelity ROM, while yielding comparable accuracy.

Nomenclature

Abbreviation	Definition
MSFR	Molten salt fast reactor
FEM	Finite element method
DGFEM	Discontinuous Galerkin Finite element method
HFM	High-fidelity model
LFM	Low-fidelity model
NTE	Neutron transport equation
PDE	Partial differential equation
POD	Proper orthogonal decomposition
aPOD	Adaptive proper orthogonal decomposition
AB-POD	Adapted Bi-Fidelity Proper Orthogonal Decomposition
FB-POD	Filtered Bi-Fidelity Proper Orthogonal Decomposition
ROM	Reduced order modeling
SVD	Singular value decomposition
Symbol	Definition
$\frac{t}{t}$	Time
σ	Singular value
e	Absolute error tolerance
γ_r	Truncation error tolerance
γ_{max}	Global error tolerance
Yint	Local error tolerance
λ_{max}	Global error tolerance for the correction factor
λ_{int}	Local error tolerance for the correction factor
ζ_{max}	Global error tolerance for the FB-POD
p	Parameter node
p	Parameter point
d	Dimension
ψ	POD mode
M	Low-fidelity snapshot matrix
Н	High-fidelity snapshot matrix
c	Coefficient of POD mode
${\cal P}$	Set of nodes
m	Number of points
l_d	Level of sparse grid along dimension d
L	Level of sparse grid
w	Hierarchical weight
${\mathcal T}$	Test set
$\mathcal C$	Candidate set
z	Important set
$\Psi(\cdot)$	Forward operator
μ	Greediness factor
\dot{x}	Union of important sets
Σ_{x}	Macroscopic cross-section
N	Number density of nuclei
σ_{χ}	Microscopic cross-section
\tilde{n}	Differential neutron density
ϕ	Angle-dependent flux
Š	Neutron source
v	Neutron speed
J	Neutron flux density
D	Diffusion coefficient
ν	Number of neutrons released per fission reaction

Contents

Abstract									
No	Nomenclature								
1	1.1	Dduction Background and Project Motivation	1 1 2						
2	2.2	, , ,	11 11 13 14 17 18 18						
3	3.1		23 23 23 25 25 26						
4	4.1 4.2 4.3	ults 3 Results Case 1: 1D Analytical Functions 3 4.1.1 Multi-grid 3 4.1.2 Multi-physics 3 Results Case 2: 2D Neutron Diffusion 3 Case study 3: 2D Neutron Transport 4	32 35 38						
5	5.1	Filtered Bi-Fidelity Proper Orthogonal Decomposition	17						
6	Conclusions and Recommendations516.1 Filtered Bi-Fidelity Proper Orthogonal Decomposition516.2 Adapted Bi-Fidelity Proper Orthogonal Decomposition516.3 Recommendations52								
Bil	bliog	raphy	53						

1

Introduction

1.1. Background and Project Motivation

Nuclear reactors provide a reliable, low-carbon source of electricity and heat, making them an attractive option for policy makers that need to reduce their countries' greenhouse gas emissions and meet climate targets. The safe and efficient operation of nuclear reactors requires accurate and high-fidelity modeling of the reactor physics. High-fidelity modeling involves detailed simulations of the behavior of neutrons and other particles in the reactor, as well as the heat transfer and fluid dynamics that occur in the reactor core. These simulations can be computationally intensive, requiring powerful computers and specialized software. Accurate modeling of reactor physics is essential to ensure the safety and reliability of nuclear reactors [2]. It allows for the optimization of reactor design and operation, and for the prediction and analysis of reactor performance under different conditions. High-fidelity modeling can also be used to investigate and address safety concerns, such as the behavior of nuclear fuel during accidents. In recent years, advancements in high-performance computing and simulation tools have enabled more detailed and accurate modeling of reactor physics. This has led to the development of advanced reactor concepts, such as small modular reactors and advanced fast reactors, which are designed to be safer and more efficient than traditional nuclear reactors [3].

Accurate and high-fidelity modeling of the reactor physics is essential to the safe and efficient operation of nuclear reactors, and to the development of advanced reactor concepts. Ongoing research and development in the field of reactor physics is critical to realise the full potential of nuclear energy as a low-carbon source of electricity and heat.

Computational power is on of these challenges when it comes to high-fidelity modeling of nuclear reactors. Detailed simulations of reactor physics involve complex calculations that require significant computing resources, which can be time-consuming and expensive. Advancements in high-performance computing has helped to address this challenge. High-performance computers and parallel processing techniques allow for faster and more efficient simulations. Additionally, the use of reduced order models can help to reduce the computational cost of simulations while maintaining a high level of accuracy. This method allows for an approximation of a complex model by only capturing the essential features, thereby reducing the computational load. When applied in a non-intrusive matter, reduced order modeling allows for the construction of surrogate models without knowledge of the underlying mathematics or access to the source code of the model, making these methods easy to implement and widely applicable in various fields of science and engineering. Ongoing research on reduced order modeling in the field of reactor physics is focused on developing new techniques and algorithms that can improve the efficiency and accuracy of simulations[3].

Multi-fidelity modeling plays an important role in the field of high-performance computing. by allowing for simulations to be performed at different levels of accuracy and computational cost. In multi-fidelity modeling, simplified models are used to provide estimates of reactor behavior at a lower computational cost, while more detailed models are used to provide more accurate results but require more com-

2 1. Introduction

putational resources. By combining these models, it is possible to perform simulations that are both accurate and efficient [4].

Multi-fidelity modeling can be particularly useful in the field of reduced order modeling as the construction of a reduced order surrogate model can still require large computational power. In the building phase, many evaluations of the complex high-fidelity model are used to capture all the dynamics of the system. This is a process that can be referred to as *training* the surrogate model. A good approximation by the reduced order model should have a small approximation error and preserve the properties of the original system. Obtaining enough high-fidelity data is not always feasible due to the computational workload. Large amounts of readily available data based on simplified models, however, can be used for training the surrogate model instead. The need for many computationally expensive high-fidelity evaluations is thereby reduced. Simplified geometry of physics-informed assumptions can be used to construct such low-fidelity models.

Overall, multi-fidelity reduced order modeling is a valuable tool in the field of nuclear reactor physics, as it allows for efficiently exploring a wide range of scenarios and design options.

1.2. Research Objective

The aim of this project is to minimize the computational workload involved in constructing a reduced order model during the offline phase. This will be achieved by decreasing the number of high-fidelity model evaluations necessary for building the reduced order model while maintaining accurate results. To this end, the existing adaptive proper orthogonal decomposition algorithm will be enhanced by employing multi-fidelity techniques. Two multi-fidelity reduced order models will be built using a filtering and an adaptation strategy. These models will be evaluated on three different test cases, and the balance between the accuracy of each multi-fidelity ROM and the computational cost, measured by the number of high-fidelity evaluations, will be investigated.

The report is structured as follows: in Section 2, the underlying theoretical framework for this study is presented. The concept of reduced order modeling and multi-fidelity strategies is explained and both existing methods and novel proposed methods are discussed. The section continues with the theory of nuclear reactor physics. Section 3 presents the numerical methods used in this work and the test cases that will be utilized to investigate the proposed multi-fidelity ROM methods. The results of the developed multi-fidelity algorithms are presented and compared to the existing adaptive proper orthogonal decomposition method in Section 4. Finally, the conclusions and recommendations for further research are given in Section 5.

Background

In this Section, the underlying theoretical framework for this study is presented. The concept of Reduced Order Modeling is introduced in Section 2.1, highlighting its significance and utility. Proper Orthogonal Decomposition, the reducing methodology utilized in this study, is then described, along with its application using sparse grids. Furthermore, it explains how the sparse grids can be refined adaptively following the work of *Alsayyari et al.* (2019). In Section 2.2, a review of previous literature on multifidelity methods and a novel approach to the adaptive sparse grid framework is presented. Section 2.2 concludes with a description of the algorithms employed in this study. Finally, Section 2.3 outlines the nuclear reactor physics theory relevant to the test cases used to evaluate the algorithms.

2.1. Reduced Order Modeling

Capturing the behavior of a complex system results in models that contain many equations or depend on many parameters, which require large computational power to evaluate. For example, describing molten salt fast reactors where the primary coolant and fuel are a molten salt mixture leading to coupled neutronics and thermal-hydraulics. Comprehensive models give insight into these multi-physics phenomena but are impractical for many query applications like uncertainty quantification or design optimization due to the required computational power. Reduced Order Modeling (ROM) allows for an approximation of a complex model by only capturing the essential features, thereby reducing the computational load. To that extent, the number of state variables, the variables used to describe the system's state, is greatly reduced in an offline phase. In this phase, many evaluations of the complex high-fidelity model are used to capture all the dynamics of the system. The order of the model can then be reduced through various techniques. A good approximation should have a small approximation error, preserve properties of the original system, and have a computationally efficient reduction method [33]. In the online phase, the ROM is employed to quickly produce accurate approximations for any range of input parameters. The speed of the online phase outweighs the computational cost of the offline part. Reduced order modeling methods can be divided into two classes: intrusive or projection-based and non-intrusive. Intrusive methods require the governing equations of the system, while non-intrusive methods build surrogate models based on the in- and output of the model without accessing the underlying equations [6].

Intrusive methods project the high-fidelity model on a reduced basis, thereby reducing the dimension of the system that has to be solved. Consider a general time-dependent Partial Differential Equation (PDE) that has to be solved for some physical quantity $\mathbf{u}(\mathbf{x},t)$ depending on state space \mathbf{x} and time t:

$$\frac{d\mathbf{u}}{dt} = \mathfrak{L}(\mathbf{u}(\mathbf{x},t)) + \mathfrak{N}(\mathbf{u}(\mathbf{x},t)), \tag{2.1}$$

where $\mathfrak{L}(\cdot)$ is a linear operator and $\mathfrak{N}(\cdot)$ is a nonlinear function. Many physical phenomena are governed by PDEs, like the propagation of heat, sound, or as in this work, neutrons, and are often come across in the science and engineering fields. Finding exact solutions of PDEs is difficult if not impossible [17].

Instead, PDEs are often solved numerically using a discretization method like finite differences or finite elements. For Equation 2.1, this yields the following form

$$\frac{d\mathbf{u}(t)}{dt} = A\mathbf{u}(t) + \Re(\mathbf{u}(\mathbf{x}, t)), \tag{2.2}$$

where $\mathbf{u}(t) \in \mathbb{R}^m$ is the spatial discretization of $\mathbf{u}(\mathbf{x},t)$, $\mathbf{A} \in \mathbb{R}^{m \times m}$ is the matrix notation of the discretization of the linear operator $\mathfrak{L}(\cdot)$, and \mathfrak{N} is a nonlinear function. To reduce the dimension of the system m, an approximation is sought by projecting the full solution onto a r-dimensional subspace, where r << m. This gives

$$\mathbf{u}(t) \approx \mathbf{u}_r(t) = V\mathbf{c}(t), \tag{2.3}$$

where the columns of $V \in \mathbb{R}^{m \times r}$ span the reduced subspace and $\mathbf{c}(t) \in \mathbb{R}^r$. Furthermore, a projection matrix W is defined such that $W^TV = I$ where $I \in \mathbb{R}^{r \times r}$ is the identity matrix. Filling Equation 2.3 into equation 2.2 and multiplying both sides with W^T results in the reduced system

$$W^{T}V\frac{d\mathbf{c}(t)}{dt} = W^{T}AV\mathbf{c}(t) + W^{T}\mathfrak{N}(\mathbf{c}(t)). \tag{2.4}$$

Once the basis matrix V and the projection W^T are computed, the computational cost of solving Equation 2.4 will be lower than solving the full-order model due to the reduced dimensionality. Projection-based model reduction is especially beneficial for linear systems as the reduced model forms a compact representation that does not require the original m-dimensional model anymore. For nonlinear terms, however, the reduced operator cannot be computed without evaluating the nonlinear operator $\mathfrak{N}(\cdot)$ which still depends on the large dimension of the original system. This reduces the effectiveness of the model reduction. Various methods of overcoming this exist like linearization of the nonlinear term [14], though, intrusive model order reduction remains an active field of research that is outside the scope of this thesis.

Data-driven or non-intrusive methods overcome the problem of non-linearity by building a surrogate model from the in- and output, treating the original model as a 'black box'. Knowledge of the underlying mathematics or access to the source code of the model is in that case not necessary, making these methods easy to implement and widely applicable [2]. A common method and the one used in this work is Proper Orthogonal Decomposition (POD).

2.1.1. Proper Orthogonal Decomposition

Proper Orthogonal Decomposition has become a popular method in the various fields of science and engineering for computing high accuracy approximations. It has been shown that for a given data set and a given number of modes, POD will provide the most optimal basis to compute an approximation in a least square sense [8]. In POD, the state vector $\mathbf{u}(\mathbf{x}; \mathbf{p}_a) \in \mathbb{R}^m$ of an complex system can be approximated at any given design parameter $\mathbf{p}_a \in \mathbb{R}^d$ by a linear combination of orthonormal basis functions or $POD \mod s \psi_i(\mathbf{x})$, that lay in some subspace with dimension r << m:

$$\mathbf{u}(\mathbf{x}; \boldsymbol{\rho}_a) \approx \hat{\mathbf{u}}(\mathbf{x}; \boldsymbol{\rho}_a) = \sum_{i=1}^r c_i(\boldsymbol{\rho}_a) \psi_i(\mathbf{x})$$
 (2.5)

where c_i are the coefficients dependent on the input parameter \mathbf{p}_a and r is the number of modes of the reduced order model. A orthonormal basis is sought that minimizes the error between the true value and the approximation in the L_2 norm [18]:

$$\min_{\psi_i} \mathbf{E} = \min_{\psi_i} \sum_{a=1}^r \left| \left| \mathbf{u}(\mathbf{p}_a) - \sum_{i=1}^{N_r} c_i(\mathbf{p}_a) \psi_i \right| \right|_{L_2}, \tag{2.6}$$

where the L_2 norm is defined as

$$\left|\left|\mathbf{u}(\mathbf{x})\right|\right|_{L_2} = \sqrt{\int_{\Omega} \left|\mathbf{u}(\mathbf{x})\right|^2 d\Omega}.$$
 (2.7)

The idea is to first determine the optimal basis that minimizes Equation 2.6 for the best approximation. Then, using the orthonormality of the basis, compute the coefficients c_i . Because the basis vectors are orthonormal, the i^{th} coefficient c_i can be calculated by taking the scalar product of the solution at the sampled points with the i^{th} basis vector:

$$c_i(\mathbf{p}_a) = \langle \psi_i, \mathbf{u}(\mathbf{p}_a) \rangle. \tag{2.8}$$

For convenience, the spatial dependence of the true solution and the basis vectors are now implied, that is $\mathbf{u}(\mathbf{x}; \mathbf{p}_a) = \mathbf{u}(\mathbf{p}_a)$ and $\psi_i(\mathbf{x}) = \psi_i$.

Different ways exist to derive the POD basis, in this work Singular Value Decomposition (SVD) is used. To that extent, a so-called *snapshot-matrix* has to be constructed,

$$\mathbf{M} = [\mathbf{u}_1, \mathbf{u}_2, ..., \mathbf{u}_n] \in \mathbb{R}^{m \times n}$$
 (2.9)

that contains n solutions or *snapshots* of the high-fidelity model for certain points in parameter space. The matrix \mathbf{M} is then deconstructed into three matrices:

$$\mathbf{M} = \mathbf{U}\Sigma\mathbf{V}^T. \tag{2.10}$$

The left singular vector matrix $\mathbf{U} \in \mathbb{R}^{m \times m}$ holds the basis vectors ψ_i , while the diagonal matrix $\Sigma \in \mathbb{R}^{m \times n}$ contains the singular values σ_h on its main diagonal. The last m-n rows of Σ contain zeros. Furthermore, the singular values are ordered such that $\sigma_1 \geq \sigma_2 \geq ... \geq \sigma_{\min\{m,n\}} > 0$. The matrix $\mathbf{V} \in \mathbb{R}^{n \times n}$ holds the right singular vectors v_i . This decomposition is proved to exist for every $m \times n$ matrix [16]. To construct the decomposition of Equation 2.10, it is assumed that $m \geq n$, though a similar procedure can be followed in the case of m < n, see [16]. Both matrices \mathbf{U} and \mathbf{V}^T are orthogonal, that is

$$\mathbf{U}^T \mathbf{U} = \mathbf{I}^{m \times m} \tag{2.11}$$

$$\mathbf{U}^T \mathbf{U} = \mathbf{I}^{n \times n} \tag{2.12}$$

where I is the identity matrix. To find U and V^T , the originality property is used to compute the following two eigenvalue problems:

$$\mathbf{M}^T \mathbf{M} \mathbf{V} = \mathbf{V} \Sigma^2 \tag{2.13}$$

$$\mathbf{MM}^{T}\mathbf{U} = \mathbf{U}\Sigma^{2} \tag{2.14}$$

Usually, the eigenvalues and eigenvectors of $\mathbf{M}^T \mathbf{M}$ are computed to find \mathbf{V} and Σ , and then matrix \mathbf{U} is obtained by direct calculation [8]:

$$\mathbf{U} = \mathbf{M}\mathbf{V}\Sigma^{-1}.\tag{2.15}$$

Once the basis vectors ψ_i are found, Equation 2.8 is used to compute the corresponding coefficients $c_i(\mathbf{p}_a)$ at the sampled parameter points \mathbf{p}_a .

To make a low-order approximation of **M**, the first r POD modes and their singular values are chosen. The matrix Σ is truncated into a square $r \times r$ matrix, and the corresponding columns of **U** and \mathbf{V}^T are kept as well [8]:

$$\mathbf{M} \approx \mathbf{U}_r \Sigma_r \mathbf{V}_r^T. \tag{2.16}$$

Limiting the number of basis vectors to represent the solution introduces a truncation error e_r . The square of the singular values σ_h^2 represents how much *energy* a POD mode contributes to the total solution. The truncation error is therefore represented as the percentage of squared singular values that are disregarded. It only measures the error in approximating the true solutions that are in the snapshot matrix. If enough samples points are taken, however, it can indicate the error of new approximations. This truncation error is controlled by keeping it smaller than a chosen threshold value γ_r [12]:

$$e_r = \frac{\sum_{h=r+1}^m \sigma_h^2}{\sum_{h=1}^m \sigma_h^2} < \gamma_r.$$
 (2.17)

The coefficients in Equation 2.8 can only be found for the points where the exact solution $\mathbf{u}(\mathbf{p}_a)$ is known. The purpose of ROM is to make quick approximations for unsampled points, without having to compute the full solution. To achieve this, the coefficients have to be interpolated for the unsampled points. Interpolation can be done through simple interpolation as in [24], using Radial Basis Functions as done in [34], by Kriging [35], or Smolyak interpolation [12]. This last method was employed for the adaptive Proper Orthogonal Decomposition by *Alsayyari et al.*, which is used in this work.

2.1.2. Sparse grids and Smolyak Interpolation

For an accurate approximation and to not miss any interesting behaviour of the system, the snapshot-matrix **M** should contain enough snapshots. An efficient approach to sampling parameter space has to be taken, because the high-fidelity model requires long computation times and the number of samples needed from such model grows exponentially with increasing dimensions. Determining the optimal number of sampling points is a key challenge, which becomes even more difficult in high-dimensional problems. To capture all dynamics of the system, uniform sampling with small intervals can be used, but it is computationally expensive. An alternative solution is to use a sparse grid, which is built by selecting a set of points for each dimension separately. Sparse grids are effective in high-dimensional problems and can be adapted to reach the desired accuracy in each dimension through a hierarchical construction of grids on top of each other [12].

To construct a sparse grid, unidimensional nodes are computed hierarchically for each dimension per level l, where the node of the highest level is assigned level l=1 and referred to as the *root node*. A *node* refers to a point along a single dimension in a multidimensional parameter space, while a *point* is a combination of nodes, one from each dimension. The j^{th} node at level l along dimension d is p_{jd}^{ld} and the set of all nodes at level l is indicated by \mathcal{P}^{ld} . Nodes from each dimension together form a point in parameter space $\mathbf{p}=(p_{j_1}^{l_1},...,p_{jd}^{l_d})$, $\mathbf{p}\in\mathbb{R}^d$. For this work nested nodes are chosen, i.e. $\mathcal{P}^{ld}\subseteq\mathcal{P}^{ld+1}$, for their efficiency, as this prevents repeating model evaluations when increasing the sparse grid level. The newly added nodes of level l+1 are in the difference set $\mathcal{P}_{\Delta}^{ld+1}=\mathcal{P}^{ld+1}\backslash\mathcal{P}^{l_d}$. For the sparse grids, the d-dimensional parameter space is mapped onto a unitary hypercube $[0,1]^d$, that can later be scaled to the physical range of the input parameters. Selecting the location of nodes can be done in various ways. To ensure optimal separations of nodes across the parameter domain, the nodes in this work are generated equidistant from each other. However, the sparse grid will be locally refined through an adaptive sampling scheme, described in Section 2.1.3.

A Smolyak interpolant is built to approximate the function c(p) so that the coefficients of Equation 2.5 can be computed for new input points. First, the unidimensional case is discussed where there are only nodes, and then the derivation is extended for the multidimensional points. The index d is dropped from the notation in this one-dimensional case. The coefficients of Equation 2.8 are evaluated at the nodes p_l^l of the set \mathcal{P}^l at level l to construct a Smolyak interpolant:

$$c(p) \approx U^{l}(c)(p) = \sum_{p_{i}^{l} \in \mathcal{P}^{l}} c(p_{j}^{l}) a_{p_{j}^{l}}^{l}(p),$$
 (2.18)

where $U^l(c)(p)$ is an operator that approximates the function c(p) and $a^l_{p^l_j}(p)$ are basis functions. Piecewise multi-linear functions are used in this work because they can be used to refine specific regions. For each node p^l_i along a certain dimension, a basis function can be constructed as

$$a_{p_1^l}^1 = 1 \quad \text{if} \quad l = 1,$$

$$a_{p_j^l}^l = \begin{cases} 1 - (m^l - 1) \cdot |p - p_j^l|, & \text{if} \quad |p - p_j^l| < \frac{1}{m^l - 1},\\ 0, & \text{otherwise,} \end{cases}$$

where m^l represents the number of nodes at level l and p_i^l are the equidistant nodes defined as:

$$\begin{split} m^l = &\begin{cases} 1, & \text{if} \quad l = 1, \\ 2^{l-1} + 1, & \text{if} \quad l > 1, \end{cases} \\ p^l_j = &\begin{cases} 0.5, & \text{for} \quad l = 1 & \text{if} \ m^l = 1, \\ \frac{j-1}{m^l-1}, & \text{for} \quad l = 1, 2, ..., m^l & \text{if} \ m^l > 1. \end{cases} \end{split}$$

The interpolant (Equation 2.18) is built by adding the terms of all nodes of level l p_j^l . Since the nodes are nested, all the terms of the interpolant of level l-1 are also present in the interpolant of level l, i.e. the interpolant at level l-1 can always be represented by the interpolant of level l:

$$U^{l-1}(c)(p) = U^{l}(U^{l-1}(c)(p)). (2.19)$$

Therefore, only the terms of the newly added nodes $p_j^l \in \mathcal{P}_{\Delta}^l$ have to be found to compute the interpolant at the next level l. The newly added terms are defined as,

$$\Delta^{l}(c)(p) = U^{l}(c)(p) - U^{l-1}(c)(p), \tag{2.20}$$

which can be written as,

$$\Delta^{l}(c)(p) = \sum_{p_{j}^{l} \in \mathcal{P}^{l}} c(p_{j}^{l}) a_{p_{j}^{l}}^{l}(p) - \sum_{p_{j}^{l} \in \mathcal{P}^{l}} (U^{l-1}(c)) a_{p_{j}^{l}}^{l}(p)$$

$$= \sum_{p_{i}^{l} \in \mathcal{P}^{l}} a_{p_{j}^{l}}^{l}(p) (c(p_{j}^{l}) - (U^{l-1}(c)))$$
(2.21)

The interpolant is built such that at level l-1, the interpolant $U^{l-1}(c)$ can exactly rebuild c(p) for the nodes of level l-1, so $c(p_j^l)-U^{l-1}(c)(p_j^l)=0$ for $p_j^l\in \mathcal{P}^{l-1}$. Therefore, the summation of Equation 2.21 has only nonzero terms for the newly added nodes $p_j^l\in \mathcal{P}_{\Delta}^l$. Now, p_j^l is redefined such that it is the j^{th} node of the difference set \mathcal{P}_{Δ}^l . Making use of the fact that the number of newly added points is $m_{\Delta}^l=m^l-m^{l-1}$, Equation 2.21 can be written as,

$$\Delta^{l}(c)(p) = \sum_{j=1}^{m_{\Delta}^{l}} a_{p_{j}^{l}}^{l}(p) \left(c(p_{j}^{l}) - U^{l-1}(c)(p_{j}^{l}) \right). \tag{2.22}$$

The unidimensional nodes can be combined onto a multidimensional sparse grid using Smolyak combination if the following condition is satisfied:

$$d \le |\boldsymbol{l}| \le L + d,\tag{2.23}$$

where l_s is the level index of dimension s, $|\boldsymbol{l}| = l_1 + l_2 + ... + l_d$ and L is the level of the sparse grid. The set of points of the sparse grid at level L becomes then,

$$B_{L,d} = \bigcup_{d \le |\boldsymbol{l}| \le L+d} (\boldsymbol{\mathcal{P}}^{l_1} \otimes \cdots \otimes \boldsymbol{\mathcal{P}}^{l_d}). \tag{2.24}$$

Points are added iteratively in a hierarchically structured way until the interpolant is accurate enough. The multidimensional variant of the difference formula of Equation 2.22 can be obtained by tensor product operation:

$$A_{L,d}(c)(\boldsymbol{p}) = \sum_{|l| \le L+d} \Delta^{l_1}(c)(p_1) \otimes \cdots \otimes \Delta^{l_d}(c)(p_d). \tag{2.25}$$

This equation can be split into two parts, the first part is the value of the interpolant up to level L-1 and the second part is the contribution to interpolant of level L,

$$A_{L,d}(c)(\boldsymbol{p}) = \underbrace{\sum_{|l| < L+d} (\Delta^{l_1}(c)(x_1) \otimes \cdots \otimes \Delta^{l_d}(c)(x_d))}_{A_{L-1,d}(c)(\boldsymbol{p})} + \underbrace{\sum_{|l| = L+d} (\Delta^{l_1}(c)(x_1) \otimes \cdots \otimes \Delta^{l_d}(c)(x_d))}_{\Delta A_{L,d}(c)(\boldsymbol{p})}.$$
(2.26)

By filling in the difference Equation 2.22 for each of the dimensions indices l_s into the second part of Equation 2.26, we can write $\Delta A_{L,d}(c)(\mathbf{p})$ as

$$\Delta A_{L,d}(c)(\boldsymbol{p}) = \sum_{|l|=L+d} \sum_{j} \left(a_{p_{j_1}^{l_1}}^{l_1}(p_1) \otimes \cdots \otimes a_{p_{j_d}^{l_d}}^{l_d}(p_d) \right) \cdot \underbrace{\left(c(p_{j_1}^{l_1}, ..., p_{j_d}^{l_d}) - A_{L-1,d}(c)(p_{j_1}^{l_1}, ..., p_{j_d}^{l_d}) \right)}_{w_i^l} (2.27)$$

where w_j^l is the hierarchical surplus [2], which is the difference between the true value of the coefficients $c(\boldsymbol{p}_j^l)$ at the newly added points and the approximation made by the interpolant $A_{L-1,d}(c)(p_{j_1}^{l_1},...,p_{j_d}^{l_d})$, based on the points of the previous level L-1. Furthermore, $\mathbf{j}=(j_1,...,j_d)$ is a multi-index to keep track of the newly added points along each dimension k. The indices run from $j_k=1,...,m_{\Delta}^{l_k}$ and k=1,...,d. An example of the generation of the interpolant is illustrated in figure 2.1.

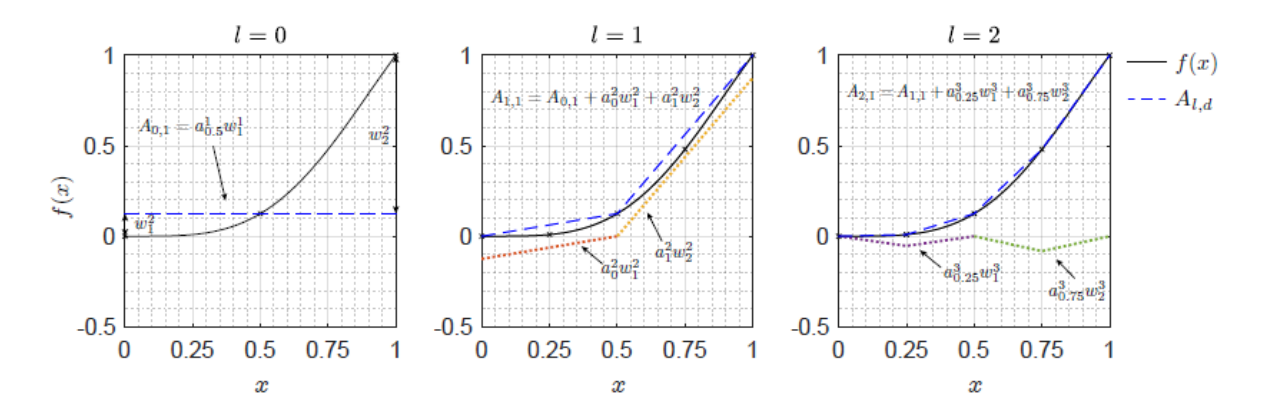


Figure 2.1: Computation of the interpolant $A_{l,d}$ for levels l=0 to l=2, where each level new terms are added to the interpolant of the previous level. These new terms are calculated using the weights w_j^L , which is the difference between the true function at the forward points and the interpolated value. The interpolant is trying to approximate a simple 1D function $f(x) = x^2 sin(\frac{\pi}{n})^2$ [2].

2.1.3. Adaptive Proper Orthogonal Decomposition

The quality of the interpolant is determined by which points in parameter space are sampled and how many. Enough points should be gathered to accurately represent the dynamics in the system, but the amount should be still low enough that the offline phase stays computationally feasible. In multidimensional problems, some dimensions affect the system more than others. Instead of uniformly refining the sparse grid along each dimension, *Alsayyari et al.* (2019) propose an adaptive sampling strategy that refines the grid locally and combined this with POD to construct an Adaptive Proper Orthogonal Decomposition (aPOD) method for reduced order modelling. A detailed description of the construction of the adaptive sparse grid can be found in [12]. The most important points are summarized in the next paragraphs.

A root node is selected halfway each dimension at 0.5 and this is labeled as level l=1. New unidimensional nodes are then generated at the boundaries of each dimension and labeled by level l=2. Following this, nodes are hierarchically generated at half the distance between the nodes from the previous level and labeled with the corresponding level number. The root point is located at (0.5,...,0.5). The unidimensional nodes are arranged in a tree-like structure, given in Figure 2.2. Each node generated at level l+1 is a child from the connected father node at l. Each node has 2 children, expect at level l=2, where the nodes only have 1 child to remain within the boundaries. Also, each node has only 1 father and the root node is its own father.

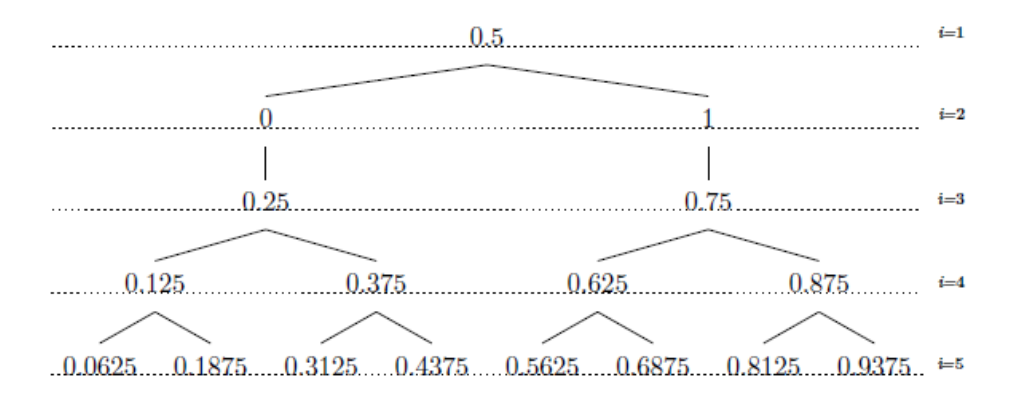


Figure 2.2: Tree structure of nodes along one dimension of the sparse grid, where l indicates the level. Each node has two children in the next level, at half the distance between the nodes of the previous level, expect at level l = 2. Here, the node has only one child [12].

By generating the children of a node along one dimension of a point, the forward points of that point are created. Since each node has two children and the parameter space is d-dimensional, each point has maximally 2d forward points. The set of forward points is the set of descendant points. Reversely, by returning the father of a node along one dimension, the backward point is created. So, a point has at most d backward points, and the line of father points up to the root point are the ancestor points of a certain point.

The adaptive sampling algorithm only computes forward points of points that are deemed important, thereby locally refining the grid around these important points. It is an iterative process that marks important points from a test set \mathcal{T}^k at each iteration k and adds them to the important set \mathcal{Z}^k . The test set is composed of the forward points of the important points of the last iteration \mathcal{Z}^{k-1} and the set of unimportant points at the previous iteration I^{k-1} , so

$$\mathcal{T}^k = \Psi(\mathcal{Z}^{k-1}) \cup I^{k-1}. \tag{2.28}$$

where $\Psi(\cdot)$ is an operator that returns the forward points of a given set. The important sets of all iterations are stored in \mathcal{X}^k , that is $\mathcal{X}^k = \cup_{h=1}^k \mathcal{Z}^h$. A point \boldsymbol{p} is marked as important if the ROM of the previous iteration cannot accurately approximate the solution at that point, so if the local error ϵ_j^k at that point is greater than a threshold γ_{int} , where the local error is defined as

$$\epsilon_j^k = \frac{\left| \left| \mathbf{u}(\boldsymbol{p}_j) - \sum_{h=1}^{r_k} A_{k,d}(c_h)(\boldsymbol{p}_j) \psi_h \right| \right|_{L_2}}{\left| \left| \mathbf{u}(\boldsymbol{p}_i) \right| \right|_{L_2}}.$$
 (2.29)

Only this criterion can lead to the premature termination of the algorithm when the true function intersects the interpolant at the forward points. Therefore, ancestry is included and the importance criterion is refined. First, the points from the test set that have a local relative error larger than the relative threshold γ_{int} are added to the candidate set \mathcal{C} :

$$C^k = \{ \boldsymbol{p}_i \in \mathcal{T}^k | \epsilon_i^k > \gamma_{int} + e \}. \tag{2.30}$$

where e is an absolute error measure to deal with small norms. Then, the candidate points with all their ancestors already included in the sparse grid \mathcal{X}^{k-1} are directly added to the important point set \mathcal{Z}_a^k .

$$\mathcal{Z}_a^k = \{ \boldsymbol{p}_i \in \mathcal{C}^k | \Gamma(\boldsymbol{p}_i) \subseteq \mathcal{X}^{k-1} \}. \tag{2.31}$$

where $\Gamma(\boldsymbol{p}_j)$ is an operator that returns the set of ancestor points of point \boldsymbol{p}_j . For the other candidate points, their missing ancestors are included in the important set \mathcal{Z}_b^k instead of the candidate points themselves. This is because the basis functions for the ancestors support a wider range in the domain. If a candidate point has an ancestor point that is also a candidate, it is then not added to the important set but added to the inactive set. This is because the error at these points is likely due to the error at the ancestor.

$$\mathcal{Z}_b^k = \{ \boldsymbol{p}_i \in \Gamma(\boldsymbol{p}_i) | \boldsymbol{p}_i \in \mathcal{C}^k, \Gamma(\boldsymbol{p}_i) \cap \mathcal{C}^k = \emptyset \land \boldsymbol{p}_i \notin \mathcal{X}^{k-1} \land \Gamma(\boldsymbol{p}_i) \subseteq \mathcal{X}^{k-1} \}$$
 (2.32)

The final important set \mathcal{Z}^k becomes then the union $\mathcal{Z}^k = \mathcal{Z}_a^k \cup \mathcal{Z}_b^k$. Lastly, a constraint is added to the test set to limit the number of points that are added, thereby tuning the number of function evaluations. A greediness factor μ is introduced that ranges from 0 to 1. A forward point is included in the test set \mathcal{T}^k if its fraction of backward points that are included in the important set \mathcal{X}^{k-1} is greater or equal that μ . So if $\mu=0$, the algorithm is greedy, and none of its backward points have to be included in the important set for the forward point to be accepted. If $\mu=1$, the algorithm is non-greedy, and a forward point is only accepted if all of its backward points are already deemed important in previous iterations.

To evaluate the approximation at iteration k, the interpolant for the coefficients at the newly sampled point have to be computed. Since the sparse grid is built by adding a level per iteration, the interpolant of Equation 2.26 is written in terms of iterations k as,

$$A_{k,d}(c)(\boldsymbol{p}) = A_{k-1,d}(c)(\boldsymbol{p}) + \Delta A_{k,d}(c)(\boldsymbol{p}), \tag{2.33}$$

$$\Delta A_{k,d}(c)(\mathbf{p}) = \sum_{n=1}^{m} w_n^k \Theta_n(\mathbf{p}), \tag{2.34}$$

where $\Theta_n(\mathbf{p})$ is the d-dimensional basis function for the point \mathbf{p} ,

$$\Theta_n(\mathbf{p}) = \prod_{s=1}^d a_{p_{n,s}^{i_s}}^{i_s}(p_s). \tag{2.35}$$

The surplus for each point $\mathbf{p}_n \in \mathbb{Z}^k$ is computed as,

$$w_n^k = c(\boldsymbol{p}_n) - A_{k-1,d}(\boldsymbol{p}_n). \tag{2.36}$$

After the important points are identified at iteration k, the new snapshots are added to the snapshot matrix, thereby changing the basis functions ψ_i that roll out of the SVD of Equation 2.10. As a consequence, the corresponding coefficients are also not equal and the interpolant based on these coefficients $A_{k,d}(c)(\mathbf{p})$ should be rebuilt. Since $A_{k,d}(c)(\mathbf{p})$ is mostly a function of weights w^k , the weights are updated instead of building the interpolant from scratch. The weights are easily updated by taking the dot product between the old and new basis functions,

$$\hat{w}_{q,g}^{k} = \sum_{i=1}^{r_{k}} w_{q,h}^{k} < \psi_{i}, \psi_{g} > \quad g = 1,...,r_{k+1},$$
(2.37)

where ψ_i are the basis functions before updating the snapshot matrix and ψ_g the basis functions from the updated snapshot matrix. After each iteration k, the weights are stored in the set \mathcal{W}^k .

where $\mathbf{u}(\mathbf{p}_j)$ is high fidelity solution for point \mathbf{p}_j and the summation term is the approximation made by the reduced order model at iteration k with r_k POD modes. The algorithm is terminated when all relative errors are below a global error threshold γ_{max} .

2.2. Multi-fidelity Methods

A reduced order model provides computationally efficient approximations of a system, but it requires many evaluations of a high-fidelity model (HFM) to capture all the dynamics. Using the adaptive sparse grid described in section 2.1.3 can reduce the number of evaluations needed, but the snapshot matrix may still be computationally expensive to compute. An alternative is to use cheap low-fidelity models (LFM) that are readily available but have limited accuracy. Multi-fidelity methods aim to combine this low-fidelity data with a limited amount of high-fidelity data to compute accurate, yet computationally inexpensive approximations. In the literature, the distinction between three model management strategies is made: filtering, adaptation, and fusion [4]. In this section, the three methods are described in detail, as well as, the proposed filtering and adaptation method applied to the adapted Proper Orthogonal Decomposition algorithm of section 2.1.3.

2.2.1. Filtering

In filtering, the high-fidelity model is only employed when the low-fidelity indicates certain sample points as important, for example when the low-fidelity model is not accurate enough or some criterion is met based on the low-fidelity evaluation. This way, the low-fidelity model guides the high-fidelity model through the parameter space and reduces the number of sampling points that have to evaluated by the high-fidelity model [4]. For example, *Peherstorfer et al.*(2016) constructed a biasing distribution for importance sampling with a computationally cheap model [5]. In importance sampling, points are drawn from a distribution that favors values that are expected to influence the output the most, with the aim to reduce the variance. In the case of [5], samples that have a greater probability to lie in the failure domain are sought after. A Markov Chain Monte Carlo scheme is presented by *Precott et al.*(2020) [31], that draws samples from a prior distribution, evaluates them with a low-fidelity model, and only acceptance of the output leads to evaluation by the high-fidelity model. The idea of pre-screening sampled parameter points by the low-fidelity function is used in this work. The adaptive sparse-grid sampling scheme described in section 2.1.3 is used for point selection, as the important point criteria only refines the grid along dimensions that improve the accuracy of the ROM.

2.2.2. Filtered Bi-Fidelity Proper Orthogonal Decomposition

Despite the adaptive sparse-grid algorithm's ability to efficiently sample parameter space, there is still oversampling reported [12]. This means that certain points are evaluated with the high-fidelity model, but they do not end up being included in the important set of points required to build the reduced order model. Some of these points originate from the initial steps, where all dimensions are searched for important points even though some parameters have minimal impact on the system. This is particularly challenging for high-dimensional systems as all dimensions have to be examined. Additionally, oversampling is inherent during the important point selection. When determining if points should be included in the important set \mathcal{Z}^k , the high-fidelity solution of the forward points $\Psi(\mathcal{Z}^{k-1})$ are computed to compare the true solution with the approximation made by the reduced order model. If it is found that the approximation was sufficient, then it was unnecessary to compute that high-fidelity solution.

To address the issue of unnecessary evaluations of the high-fidelity model, a Filtered Bi-Fidelity Proper Orthogonal Decomposition (FB-POD) method is proposed in this work that utilizes the efficient grid search of the adaptive Proper Orthogonal Decomposition algorithm. The sparse grid search of *Alsayyari et al.* lends itself well to the filtering method due to its locally refining nature and identification of important points through error tolerances. The criteria of Equations 2.31 and 2.32 ensure that the important set only contains input points that support the approximation of the high-fidelity solution, which makes them potential filter criteria. This filtering approach, which involves utilizing an adaptive sparsegrid to search for sample points and filtering out important points based on specific error criteria and ancestry, has not yet been demonstrated in the literature.

The proposed approach involves first building a sparse grid using a less computationally expensive low-fidelity model, following the procedure outlined in section 2.1.3. Once the low-fidelity ROM converges and the global error is below the threshold at a given iteration k, the set of important points \mathcal{X}_k is transferred to the high-fidelity model. These points will be evaluated in high fidelity to compute the high-fidelity snapshot matrix \mathbf{H} . This matrix is then used to construct the final ROM. By using the low-

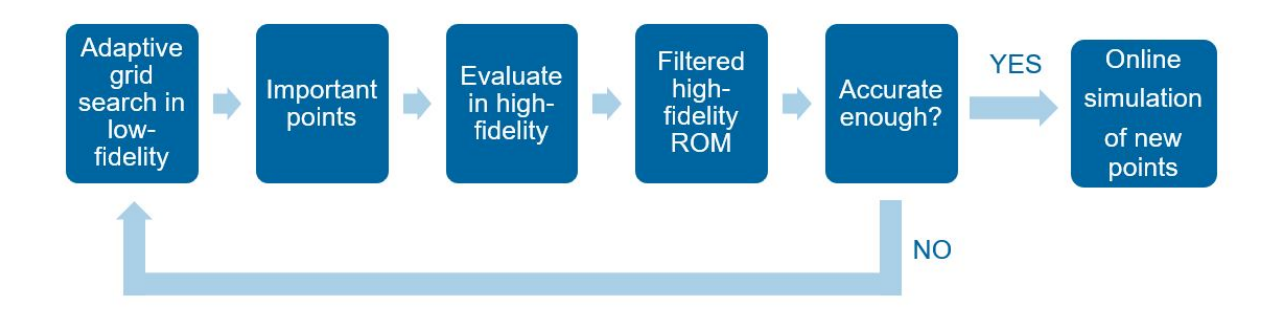


Figure 2.3: Block diagram representation of the Filtered Bi-Fidelity Proper Orthogonal Decomposition method proposed in this work.

fidelity model to filter out important points, this method eliminates the need for unnecessary evaluations of the high-fidelity model. If the high-fidelity model has significantly longer computation time than the low-fidelity equivalent and oversampling is large, significant speed-up is expected by only evaluating the important points in the high-fidelity setting. Additionally, since the points are hierarchical, with the top level points supporting more of the domain, the important points are fed in a level-by-level manner. The set of to-be-evaluated points at iteration h is then given by

$$\mathcal{T}^h = \mathcal{Z}^h \tag{2.38}$$

where $\mathcal{X}^k = \cup_{h=1}^k \mathcal{Z}^h$. Since points of a deeper level only provide local refinement, e.g. adding terms to the interpolant of the previous level, the filtered ROM is tested after each iteration to check if it can already provide an accurate approximation of the important points of the next level. If the high-fidelity ROM is already accurate enough at a particular level,

$$\epsilon_j^h < (\zeta_{max} + e) \quad \forall \boldsymbol{p}_j^{h+1} \in \mathcal{T}^{h+1},$$
 (2.39)

where ζ_{max} is a set relative global tolerance and e is again a small absolute error, the feeding of important points is prematurely terminated to avoid unnecessary evaluations. If the high-fidelity model does not converge after all important points have been fed, tighter error bounds and a higher greediness factor can be tested using the low-fidelity model to capture more of the system's dynamics. The solutions of the sampled low- and high-fidelity solutions can be recycled to keep the number of evaluations low. The pseudo-algorithm can be found in Algorithm 1 on the next page. In Figure 2.3, a block diagram of the proposed method is presented.

It is assumed that the important points of the high- and low-fidelity models share their locations in parameter space. It is therefore assumed that similar POD modes are present in both models and that the dependence of the corresponding coefficients on the parameters is also similar, i.e. both models contain the same information. This assumption is reasonable for models that have the same set of input parameters to describe the same system but differ in non-physical properties like numerical solver. However, models of different fidelity may be influenced by other input parameters, by the same input parameters in different ways, or contains other dynamics. The important point selection of the low-fidelity model will not capture all the physical behavior that is present in the high-fidelity model. This makes the applicability of the filtered aPOD model specific. In this work, three test cases utilizing different types of variable fidelity are tested. These three test cases are described in detail in Section 3.2.

Algorithm 1: Filtered Bifidelity Adaptive Proper Orthogonal Decomposition

```
Initialize: Run aPOD algorithm of section 2.1.3 to
 obtain X^k
Input: f_{HF}, \mathcal{X}^k, \zeta_{max}, e
Output: \mathcal{W}^h, U
Set iteration h = 1
Generate the first point Z^1 = 0.5^d
Evaluate the first sparse grid point in high-fidelity
» \mathbf{u}_{HF,1}
Add \mathbf{u}_{HF,1} to snapshot matrix
» H = [u_{HF,1}]
Compute SVD on H to obtain POD modes and
 truncate
\mathbf{v} \mathbf{U}_1 = [\psi_1^1]
Determine coefficients
 c_i^1(0.5,...,0.5) = \langle \psi_i^1, \mathbf{u}_{HF,1}(0.5,...,0.5) \rangle
Set initial weights w_i^1 = c_i^1
for h = 2 : k do
    Evaluate the function at the next level points
      p_i^h \in \mathcal{Z}^h in high-fidelity
    » \mathbf{u}_{HF,h}
    Compute interpolant A_{h-1,d}(c) for c_i(\mathbf{p}_i^h) using
    Find the error at points p_i^h as given in Equation
     2.29
    \epsilon_i^h
    if all(\epsilon_i^h < \zeta_{max} + e) then
        \mathbf{U} = \mathbf{U}_{h-1}
        break
    end
    Add \mathbf{u}_{HF,h} to snapshot matrix
    Compute SVD to obtain new modes and truncate
    » \mathbf{U}_h = [\psi_1, ..., \psi_r]
    Update the weights using Equation 2.37
    » \hat{w}_i^h
    Recompute the interpolant at the new points
    A_{h,d}(c)
    Find the new surpluses using Equation 2.36
    \gg W_i^h
    Store weights
    \mathcal{W}^h = [\mathcal{W}^{h-1}, w_i^h]
    h = h + 1
end
```

2.2.3. Adaptation

Adaptation multi-fidelity techniques enhance the output of low-fidelity methods with more accurate information from high-fidelity models during computation. A common strategy is to build a correction model for the low-fidelity model by comparing the low- and high-fidelity solutions for sample points. The correction can be additive, which is based on the difference between the low-fidelity model $f_{LF}(\mathbf{x})$ and the high-fidelity model $f_{HF}(\mathbf{p})$

$$f_{HF}(\mathbf{p}) = f_{LF}(\mathbf{p}) + C_1(\mathbf{p}). \tag{2.40}$$

or multiplicative, which uses the ratio between the low- and high-fidelity output,

$$f_{HF}(\mathbf{p}) = C_2(\mathbf{p}) f_{LF}(\mathbf{p}). \tag{2.41}$$

The correction terms C_1 and C_2 can be found, respectively, by subtraction or division of the high- and low-fidelity results;

$$C_1(\mathbf{p}) = f_{HF}(\mathbf{p}) - f_{LF}(\mathbf{p}) \tag{2.42}$$

$$C_2(\mathbf{p}) = \frac{f_{HF}(\mathbf{p})}{f_{LF}(\mathbf{p})}. (2.43)$$

The information on the correction factors at the sampled points is combined to compute corrections factors at new unsampled locations in parameter space. Adaptation methods differ in the way that the correction factor for new samples point is generated. Typically, Taylor series expansion based on gradients or higher-order derivatives is used for this [4]. If information on derivatives is not available, an approximation can be made, for example, by using finite difference like is done in [11]. These firstand second-order approaches are local to the current point and do not use the solutions from previous points. Instead, Kriging-based methods have been explored for the construction of the correction factor [15, 29]. In Kriging, information from all sampled points is used and weights are assigned based on the distance of the sampled points and the to-be-approximated point. Since the right choice between an additive and a multiplicative correction is case dependent and generally not known beforehand, Gano et al. (2005) proposed a hybrid scaling model that combines the additive and multiplicative corrections using a weighted sum [15]. They concluded, however, that a hybrid model does not outperform the additive or multiplicative corrections, but rather removes the need to choose between them beforehand. In the context of proper orthogonal decomposition, an additive correction factor has been computed by a ROM in [7]. The ROM was built using a snapshot matrix filled with snapshots of the correction surfaces at sampled points during the offline phase. In the online phase, new points are simulated by a low-fidelity evaluation and a ROM produced correction factor. A similar approach to multi-fidelity reduced order modeling will be used in this work and is described in detail in Section 2.2.4.

2.2.4. Adapted Bi-Fidelity Proper Orthogonal Decomposition

To utilize the information of the high-fidelity snapshot more efficiently and to remove the need to determine the ratio of high- and low-fidelity data beforehand as in most adaptation techniques, the adaptation multi-fidelity strategy is applied to the aPOD reduced order model, giving rise to the Adapted Bi-Fidelity Proper Orthogonal Decomposition AB-POD. To that extent, a reduced order model is made based on the additive correction factor as defined in Equation 2.42. The true correction factor is approximated by the linear combination of basis functions, as

$$\mathbf{C}(\mathbf{p}) \approx \hat{\mathbf{C}}(\mathbf{p}) = \sum_{i=1}^{r} b_i(\mathbf{p}) \boldsymbol{\phi}_i. \tag{2.44}$$

where ϕ_i are the POD modes and $b_i(\mathbf{p})$ the corresponding coefficients. To obtain these basis vectors, a snapshot matrix is filled using the same adaptive grid search as described in section 2.1.3. The points of the test set \mathcal{T}^k at iteration k are now evaluated twice: by the high- and low-fidelity model. An additive correction factor $\mathbf{C}(\mathbf{p}_j)$ is obtained for each of the points and added to the snapshot matrix \mathbf{S} instead of the solutions themselves:

$$\mathbf{S} = [\mathbf{C}_1, ..., \mathbf{C}_n]. \tag{2.45}$$

Singular value decomposition is applied to the matrix \mathbf{S} and the POD modes and coefficients are obtained. The same procedure of building an approximation for the test points \mathcal{T}^k at each iteration k and comparing it to the true solution to find the important points as in section 2.1.3 is followed. Now the true solution and approximation for the correction factor are compared. Two additional error tolerances are defined: the local relative error tolerance for the selection of important points to compute the approximation for the correction factor λ_{int} and a global relative error tolerance to stop the iterations of building the ROM for the correction factor λ_{max} . For points to be now added to the candidate set \mathcal{C}^k , the relative error of the correction factor has to be smaller than λ_{int} , so

$$C^K = \{ \boldsymbol{p}_i \in \mathcal{T}^k | \xi_i^k > \lambda_{int} + e \}, \tag{2.46}$$

where e is again a small absolute error and ξ_j^k is the local relative error of point \mathbf{p}_j at iteration k, defined as

$$\xi_j^k = \frac{||\mathbf{C}(\mathbf{p}_j) - \hat{\mathbf{C}}(\mathbf{p}_j)||}{||\mathbf{C}(\mathbf{p}_j)||_{L_2}}.$$
(2.47)

If all error ξ_j^k are below a global error tolerance λ_{max} or if no new important points are computed, the reduced order model has converged and can make accurate enough approximations of the correction factor for unsampled points. Now, it's time to build the final ROM to approximate the high-fidelity solution. The snapshot matrix **M** will be filled with corrected solutions of the low-fidelity model to mimic high-fidelity solutions,

$$\mathbf{M} = [\hat{f}_1, ..., \hat{f}_n] \tag{2.48}$$

where,

$$\hat{f}(\boldsymbol{p}_i) = f_{LF}(\boldsymbol{p}_i) + \hat{C}(\boldsymbol{p}_i). \tag{2.49}$$

The same procedure is followed of section 2.1.3, but now $\hat{f}(\boldsymbol{p}_j)$ has replaced the role of the true high-fidelity solution $\mathbf{u}(\boldsymbol{p}_j)$. The main idea is that the dependence of the correction factor on the input parameters is easier to learn than the solution itself, as thus it is assumed that the correction field is more regular than the solutions. Once a ROM is made of the correction factor, the online phase can consist of computing low-fidelity solution of new input points and correcting them with an approximated correction factor, like is done in [7]. However, the low-fidelity model can still be too computationally expensive to evaluate many times in an online phase. Therefore, in this work, the low-fidelity solutions with a correction factor are recycled into a second snapshot matrix, and a final reduced order model is computed based on corrected low-fidelity solutions. The proposed method is expected to produce an adapted MF ROM that can accurately approximate the high-fidelity model quickly in the online phase and has a computationally less intensive offline phase compared to the high-fidelity ROM. The use of non-intrusive reduced-order techniques based on POD and adaptive sparse grids with corrected low-fidelity models is a novel approach in the field and may prove helpful when constructing a high-fidelity ROM is prohibitively computationally expensive and abundant low-fidelity data is available. The pseudo-algorithm is presented in Algorithm 2 on the next page.

In the case of different discretizations of both models, the low-fidelity model is interpolated to match the discretization of the high-fidelity model using MATLAB's modified Akima cubic Hermite interpolation. A piecewise function of polynominals of at most degree three is constructed using the values of the directly neighboring grid points in every dimension. The coefficients of the polynomial are chosen such that the function passes through the given data points and satisfies the specified derivatives. This method was chosen because the interpolation method secures continuity of the first derivatives at the data points, resulting in a smooth curve. Also, it only uses information from the neighboring points to determine the interpolation coefficients, which makes the method computationally efficient. Moreover, this method has less fluctuations compared to spline interpolation. The method was modified to avoid overshoots [1, 20, 28]. Other interpolation techniques can be explored, but are not in the scope of this thesis due to time constraints.

Algorithm 2: Adapted Bi-Fidelity Proper Orthogonal Decomposition

```
Input: f_{LF}, f_{HF}, \lambda_{int}, \lambda_{max}, e Output: W^k, X^k, U
Generate the first point 0.5<sup>d</sup>
Evaluate the first sparse grid point in HF and LF
» \mathbf{u}_{H}^{1} and \mathbf{u}_{L}^{1}
Check size compatibility
Interpolation of \mathbf{u}_L^1 if needed using Akima interpolation
Calculate correction factor
» C^1 = u_H^1 - u_L^1
Add C1 to snapshot matrix
Compute SVD on C to obtain POD modes and truncate
Obtain coefficients b_i by projection
Initial weights w_{C,i}^1 = b_i
Save initial weights W_C^1 = w_{C,i}^1
First important point Z^1 = 0.5^d
Set iteration k = 1
while any(\xi_j^k > \lambda_{max} + e) do
    k = k + 1
    Generate forward points \Psi(\mathbb{Z}^{k-1})
    Construct test set \mathcal{T}^k
    Evaluate the function in the test set in LF and HF
    \mathbf{u}_{H}^{k} \& \mathbf{u}_{L}^{k}
    if size(u_H^k) \neq size(u_L^k) then
     interpolate u<sup>k</sup>
    end
    Compute the correction factor at the test points \mathbf{p}_{i}^{k} \in \mathcal{T}^{k}
    Compute the POD coefficients b_i(\mathbf{p}) at the test points via Smolyak interpolation using
     weights W^{k-1} and Equation 2.18
    Find the error at each test point using Equation 2.47
    if all(\xi_j^k < \lambda_{max} + e) then
     ∣ breák
    end
    Find important points
    Add corrections of forwards points \mathcal{C}_{fw_k} to snapshot matrix
    Compute SVD on S to obtain new POD modes
    Update weights using Equation 2.37
    Recompute the approx solution at the important points
    Find the new surpluses using Equation 2.36 and save
    \mathcal{W}_{C}^{k} = [\mathcal{W}_{C}^{k-1} w_{C,i}^{k}]
end
, Set iteration m=1
Generate the first point 0.5^d
while any(\epsilon_j^m > \gamma_{max} + e) do m = m + 1
    Generate forward points
    Construct test set \mathcal{T}^m
    if p<sup>m</sup> already evaluated in previous loop then
        Reuse LF solution u<sub>1</sub> from previous loop
        Else Evaluate the function at the forward points in LF
    Interpolate correction C from weights and anchor points from the previous loop
    \hat{y}_i^m = y_{L,i}^m + \hat{C}_i^m
    Find the error in every point using Equation 2.29
    if all(\xi_i^m < \lambda_{max} + e) then
        \mathbf{U} = \mathbf{U}^m
        break
    end
    Find important points
    Add corrections û to snapshot matrix M
    Compute SVD on M to obtain new POD modes
    Update weights using Equation 2.37
    Recompute the approx solution at the important points
    Find the new surpluses using Equation 2.36 and save
    \mathcal{W}^k = [\mathcal{W}^k, w_i^{m+1}]
end
```

2.2.5. Fusion

The final multi-fidelity strategy is fusion. With this method, models of different fidelities are evaluated separately and the information from all outputs is fused together, most commonly by exploring the cross-correlations between low- and high-fidelity models. Many of these models are based on Gaussian process regression, or Kriging, in combination with the linear auto-regressive information fusion framework by Kennedy & O'Hagan [21]. In Kriging, results for unsampled points are obtained by constructing a weighted sum of values of neighboring points. The weights are determined by covariance functions. For example, *Dong et al.*(2015) [10] proposes a fusion of information from low- and high-fidelity models based on the Kalman filter. For the Kalman filter, optimal estimates at some time step t are found by combining the observation at the previous time step and a prediction for the current time step. The surrogate model proposed in [10] disregards the time dependence and only combines the output of two different fidelity models. The predicted results are replaced by the output of the low-fidelity model Y_{LF} , while the high-fidelity model result Y_{HF} places the result at the previous time step.

Furthermore, in recent years artificial neural networks have been developed to accomplish multi-fidelity. They overcome problems other methods might encounter when approximating discontinuous functions, high dimensional problems, or strong nonlinearities [36]. The name neural comes from the fact that these networks mimic the function of a human brain and contain artificial neurons called nodes. These nodes are organized into different layers, starting with an input layer, one or multiple hidden layers, and an output layer. The nodes of the input layers are connected to nodes of the next layer through weights, where larger weights result in more influence of that input node on the output of the connected node. Neural networks can be trained to learn the relationship between low- and high-fidelity data. They can be applied in a filtering context where inexpensive low-fidelity data is used to train a neural network and when its performance does not improve anymore, the switch is made to the high-fidelity model [32]. Adaptation strategies have also been employed, where multiple neural networks are trained with varying fidelity data and are then coupled to discover their relationship [23, 30].

Lastly, Perron et al. (2022) proposed a multi-fidelity reduced-order modeling approach using Manifold alignment in recent work. This method projects the solutions of low- and high-fidelity models onto a common low-dimensional subspace, allowing for different solution sizes. The approach utilizes Proper Orthogonal Decomposition as the reduced order modeling technique, with the POD modes obtained through Singular Value Decomposition, similar to this work. In their approach, the basis functions and corresponding POD coefficients for the low- and high-fidelity data sets are obtained independently. The approach aims to transform the coefficients of the low-fidelity data set to match those of the high-fidelity set, thereby increasing the number of coefficients available for interpolation in the online phase. Procrustes analysis is used to align the coefficients of the shared data points. Once the alignment parameters are found, the coefficients of unlinked points in the low-fidelity set are shifted to optimally align with those of the high-fidelity set. The information from both POD coefficient sets is combined to obtain Hierarchical Kriging models. These models are used in the online phase together with the high-fidelity POD modes to obtain approximations for new points[9].

The employment of neural networks and manifold alignment in multi-fidelity methods are both still quite novel and could be an interesting path to explore.

2.3. Nuclear Reactor Physics

In this section, the basic principles of nuclear reactor physics that are used for this work are explained. A short introduction to neutron interactions is given, followed by the derivation of governing equations.

2.3.1. The Neutron Transport Equation

Neutrons play the crucial role of inducing fission reactions in nuclear reactors. Therefore, it is important to study their behavior in reactor physics. Neutrons travel in straight lines through media, with their paths affected by scattering and absorption due to collision with nuclei. Furthermore, neutrons can be absorbed by nuclei they come across. The probability of interaction between a neutron and one nucleus is captured in the microscopic cross-section σ_x , where x stands for the type of interaction. The cross-sections are usually dependent on the neutron energy and the type of reaction. Most of the time, the interactions that happen within 1 cm^3 of material are considered. The number of a certain reaction per cubic centimeter is obtained by multiplying the microscopic cross-section with the number nuclei in 1 cm^3 material, namely the number density N:

$$\Sigma_{x} = N\sigma_{x} \tag{2.50}$$

where Σ_x is the macroscopic cross-section for a certain reaction x. This macroscopic cross-section indicates the probability of such interaction per unit path length.

Not the individual neutrons are studied, but rather the statistical behavior of many neutrons and their distribution over the reactor. This distribution of neutrons is described by the neutron transport equation (NTE), an equation based on the balance between neutron loss and gain over time. While the neutron distribution is fully described by the differential neutron density $n(\underline{r}, E, \underline{\Omega}, t)$, in nuclear reactor physics the angle-dependent flux $\phi(r, E, \Omega, t)$ is preferred instead:

$$\phi(r, E, \Omega, t) = n(r, E, \Omega, t)v \tag{2.51}$$

where v is the neutron speed. The angle-dependent flux represents the number of neutrons that pass through a unit area perpendicular to its direction $\underline{\Omega}$ per unit time. The total number of neutrons in an arbitrary volume V, enclosed by surface S, with an energy between E and E+dE, and with direction in the solid angle $d\Omega$ around Ω , is equal to

$$\int_{V} n(r, E, \Omega, t) dV dE d\Omega \tag{2.52}$$

This number of neutrons can increase over time if a source is present, including fission. The source $S(r, E, \Omega, t)$ is defined so that the increase of neutrons is

$$\int_{V} S(r, E, \Omega, t) dV dE d\Omega.$$
 (2.53)

As neutrons travel through the medium, interactions occur between the neutrons and the atoms of the medium, such as scatter or capture. The probability of neutrons with other energies and directions scattering into the defined energy range dE and $d\Omega$ can be defined as the macroscopic cross-section $\Sigma_s(r,E'\to E,\Omega'\to\Omega)$. When integrating over all possible energies and angles from which neutrons can scatter in, the increase of neutrons due to this in-scattering becomes

$$\int_{V} \int_{0}^{\infty} \int_{4\pi} \Sigma_{s}(r, E' \to E, \Omega' \to \Omega, t) \phi(r, E', \Omega', t) dE' d\Omega' dV dE d\Omega.$$
 (2.54)

Leakage or net outflow of volume V can also occur, which is given by

$$\int_{S} n \cdot \Omega \phi(r, E, \Omega, t) dE d\Omega dS = \int_{V} \nabla \cdot \Omega \phi(r, E, \Omega, t) dV dE d\Omega, \tag{2.55}$$

where the divergence theorem of Gauss is used [19].

The probability of undergoing any interaction that leads to a decrease in the number of neutrons is given by the total macroscopic cross-section Σ_t . The number of neutrons that is lost due to this is given by

$$\int_{V} \Sigma_{t}(r, E)\phi(r, E, \Omega, t)dVdEd\Omega. \tag{2.56}$$

Adding these various positive and negative contributions gives the change in number of neutrons over time:

$$\frac{\partial}{\partial t} \int_{V} n(r, E, \Omega, t) dV dE d\Omega = \int_{V} S(r, E, \Omega, t) dV dE d\Omega$$

$$+ \int_{V} \int_{0}^{\infty} \int_{4\pi} \Sigma_{S}(r, E' \to E, \Omega' \to \Omega, t) \phi(r, E', \Omega', t) dE' d\Omega' dV dE d\Omega$$

$$- \int_{V} \Sigma_{t}(r, E) \phi(r, E, \Omega, t) dV dE d\Omega.$$
(2.57)

When substituting equation 2.51 into equation 2.57, the latter can be rewritten to:

$$\int_{V} \left(\frac{1}{v} \frac{\partial \phi(\underline{r}, E, \underline{\Omega}, t)}{\partial t} - S(\underline{r}, E, \underline{\Omega}, t) - \int_{0}^{\infty} \int_{4\pi} \Sigma_{s}(\underline{r}, E' \to E, \underline{\Omega'} \to \underline{\Omega}) \phi(\underline{r}, E, \underline{\Omega}, t) dE' d\Omega' + \underline{\Omega} \cdot \nabla \phi(\underline{r}, E, \underline{\Omega}, t) + \Sigma_{t}(\underline{r}, E) \phi(\underline{r}, E, \underline{\Omega}, t) \right) dV = 0$$
(2.58)

This integrand should be zero, as equation 2.58 has to hold for every volume V. This last step yields the linear integro-differential equation for the angle-dependent neutron flux, known as the neutron transport equation:

$$\frac{1}{v} \frac{\partial \phi(\underline{r}, E, \underline{\Omega}, t)}{\partial t} = S(\underline{r}, E, \underline{\Omega}, t) + \int_{0}^{\infty} \int_{4\pi} \Sigma_{S}(\underline{r}, E' \to E, \underline{\Omega'} \to \underline{\Omega}) \phi(\underline{r}, E, \underline{\Omega}, t) dE' d\Omega' \\
-\underline{\Omega} \cdot \underline{\nabla} \phi(\underline{r}, E, \underline{\Omega}, t) - \Sigma_{t}(\underline{r}, E) \phi(\underline{r}, E, \underline{\Omega}, t) \tag{2.59}$$

In this thesis, the time-independent version of the *one-speed* neutron transport equation is solved, which is obtained by assuming steady-state, i.e. $\partial \phi/\partial t=0$, and assuming all neutrons have the same energy. Though in reality neutrons occur with a spectrum of energies that changes by scattering collisions, the energy dependence can be dropped by only considering mono-energetic neutrons:

$$S(\underline{r},\underline{\Omega}) + \int_{4\pi} \Sigma_{s}(\underline{r},\underline{\Omega'} \to \underline{\Omega})\phi(\underline{r},\underline{\Omega})d\Omega'$$

$$= \underline{\Omega} \cdot \underline{\nabla}\phi(\underline{r},\underline{\Omega}) + \Sigma_{t}(\underline{r})\phi(\underline{r},\underline{\Omega}).$$
(2.60)

2.3.2. Neutron Diffusion Theory

Solving the neutron transport equation analytically is very difficult, even for the simplest of cases. Instead, assumptions are made to simplify equation 2.59. The first assumption is considering only monoenergetic neutrons,

$$\frac{1}{v} \frac{\partial \phi(\underline{r}, \underline{\Omega}, t)}{\partial t} = S(\underline{r}, \underline{\Omega}, t) + \int_{4\pi} \Sigma_{s}(\underline{r}, \underline{\Omega'} \to \underline{\Omega}) \phi(\underline{r}, \underline{\Omega}, t)' d\Omega' \\
-\underline{\Omega} \cdot \underline{\nabla} \phi(\underline{r}, \underline{\Omega}, t) - \Sigma_{t}(\underline{r}) \phi(\underline{r}, \underline{\Omega}, t).$$
(2.61)

Furthermore, the neutron flux density J(r, E, t) represents the net number of neutrons that flows through a surface dS per unit time, and is defined as

$$\underline{\underline{J}(\underline{r},E,t)} = \int_{4\pi} \underline{\Omega} \phi(\underline{r},E,\underline{\Omega},t) d\underline{\Omega}$$
 (2.62)

Substitution of the neutron flux density into equation 2.61 and integrating over Ω gives

$$\frac{1}{v}\frac{\partial}{\partial t}\phi(\underline{r},t) = -\underline{\nabla}\cdot\underline{J}(\underline{r},t) - \Sigma_a(\underline{r}\phi(\underline{r},t) + S(\underline{r},t))$$
 (2.63)

where Σ_a is the macroscopic absorption cross-section and $\Sigma_a = \Sigma_t - \Sigma_s$. A final diffusion approximation is made to arrive at the diffusion equation. It is assumed that the neutron current density $\underline{J}(\underline{r},t)$ is proportional to the negative of the gradient of the neutron flux $\underline{\nabla}\phi(\underline{r},t)$, meaning that neutrons diffuse from high density areas to low density. The proportionality constant is called the diffusion coefficient D(r). This assumption is referred to as Fick's Iaw [19],

$$J(\underline{r},t) \approx -D(\underline{r})\underline{\nabla}\phi(\underline{r},t). \tag{2.64}$$

Substitution of equation 2.64 in 2.63 yields the final diffusion equation:

$$\frac{1}{v}\frac{\partial}{\partial t}\phi(\underline{r},t) = \underline{\nabla}\cdot D(\underline{r})\underline{\nabla}\phi(\underline{r},t) - \Sigma_a(\underline{r}\phi(\underline{r},t) + S(\underline{r},t)$$
 (2.65)

By making assumptions about the angle dependence of neutron flux, the diffusion equation is not valid at places with strongly differing properties or in strongly absorbing media. This implies that the solution that follows from the diffusion equation may deviate from the more accurate solution of the transport equation when external neutron sources and interfaces are present.

In this thesis, the fixed source equation will be solved, meaning that it is assumed that there is no time dependence and there is a fixed source S(r). The time-independent diffusion equation then becomes,

$$\underline{\nabla} \cdot D(\underline{r})\underline{\nabla}\phi(\underline{r}) - \Sigma_a(\underline{r}\phi(\underline{r}) + S(\underline{r}) = 0. \tag{2.66}$$

Furthermore, the source is split into an external source and a fission source

$$S = S_{ext}(\underline{r}) + S_f \tag{2.67}$$

where $S_f = \nu \Sigma_f(\underline{r}) \phi(\underline{r})$ is the fission source, ν is the number of neutrons released per fission reaction, and Σ_f is the macroscopic fission cross-section. By substituting equation 2.67 into the time-independent diffusion equation, the source driven one-group diffusion equation is obtained,

$$\nabla \cdot D(r)\nabla\phi(r) - \Sigma_a(r\phi(r) + \nu\Sigma_f(r)\phi(r) + S_{ext}(r) = 0.$$
 (2.68)

2.3.3. Molten Salt Fast Reactor

Renewable energy sources have been the topic of discussion in politics and science for many years now. With the increasing global population and economic growth among all continents, the rising demand for energy not expected to slow down and alternatives to fossil fuels should be explored. The Generation IV International Forum (GIF) selected the Molten Salt Fast Reactor (MSFR) as one of the Generation IV reactors. Their goal is to develop research on feasibility and performance of the reactor, and enable deployment of the reactor in industry by 2030 [13]. In a MSFR, liquid salt is not only used as fuel, but also functions as a coolant. The design is considered to be inherently safe due the strong negative temperature feedback coefficient and freeze-plug safety mechanism. Moreover, the MSFR can consume waste from other conventional reactors [27]. The safety and sustainability aspects make this type of reactor an attractive candidate for future energy supply. Currently, MSFR research projects focuses on physical, chemical, and material studies to obtain the optimal system configuration for the reactor core, waste conditioning, and reprocessing unit. Some of the research and development objectives include, chemical and thermodynamic properties of salts, advanced neutronic and thermalhydraulic coupling models, salt redox control technologies, and safety assessment [13]. Analyzing these objectives requires computational heavy high-fidelity models with multiple input parameters and intertwined neutronics, fluid dynamics and heat transfer [3]. ROM techniques can be applied to simplify these problems and produce an efficient, cheap, and accurate model of the system. Moreover, multi-fidelity methods introduced in Section 2.2 can possibly relieve some of the computational burden for the construction of the ROMs by decreasing the number of high-fidelity evaluations.

Summary

This concludes the theoretical background of this study, detailing how non-intrusive reduced-order modeling techniques can overcome computational barriers in modeling complex systems like nuclear reactors. Section 2.1 serves as the mathematical foundation for the multi-fidelity methods proposed in this work. Multi-fidelity strategies can aid in reduced order modeling, as discussed in Section 2.2. Section 2.2 includes a literature review of multi-fidelity approaches in filtering, adaptation, and fusion. Additionally, Section 2.2 describes the two novel approaches to applying multi-fidelity in proper orthogonal decomposition, namely the Filtered and Adapted Bi-Fidelity Proper Orthogonal Decomposition algorithms. The FB-POD and AB-POD algorithms will be used to approximate solutions to the neutron diffusion and transport equations discussed in Section 2.3.1 for specific geometries, which will be described in detail in the next section.

Methods

In this section, the numerical methods and test cases to study the proposed filtering and adaptation bi-fidelity methods of Section 2.2.2 and 2.2.4 are described. Section 3.1.1 describes the Finite Element Method that is used to approximate the solutions to the neutron diffusion and transport equations of Section 2.3.1. Then, Section 3.1.2 describes the Space-Angle Discontinuous Galerkin Method, which is used for computing the numerical solutions of the neutron transport equation in this work. This section concludes with a detailed description of three test cases in Section 3.2. The three test cases differ in the problem definition, solver, and variable fidelity strategy, and will be used to study the accuracy and computational burden of the proposed Filtered and Adapted Bi-fidelity Proper Orthogonal Decomposition.

3.1. Numerical Methods

3.1.1. Finite Element Method

Most complex problems cannot be solved analytically with partial differential equations due to their geometry or non-linearities. Instead, discretization methods are used to approximate the system and solve the equations numerically. One such method is the Finite Element Method (FEM), which divides a complex space into finite number of elements described by simple equations to solve boundary value problems [25].

FEM involves dividing a complex physical system or structure into smaller, simpler sub-components called finite elements. These elements are small, geometrically simple shapes, such as triangles or rectangles, that can be easily analyzed. Mathematical equations are developed to describe the behavior of each element, typically involving the physical properties of the element, such as material properties and boundary conditions. The equations for each element are combined into a larger system of equations that describe the behavior of the entire system. The system of equations is solved numerically using a computer algorithm to approximate the solution of the entire system.

In the context of nuclear reactors, FEM is commonly used to simulate and analyze the behavior of reactor components and systems under various operating conditions [26]. This includes the behavior of fuel rods, reactor pressure vessels, coolant systems, and other critical components.

3.1.2. Space-Angle Discontinuous Galerkin Method

Numerical solutions of the neutron transport equation have been a topic of research for over 50 years due to the high dimensionality of the problem. This work uses the in-house code PHANTOM-DG, which is based on a space-angle Discontinuous Galerkin Finite Element Method (DGFEM) approach with local angular refinement developed by J. Kópházi and D. Lathouwers. Here the method is summarized, and the detailed explanation can be found in [22].

The spatial domain V is discretized in elements V_k , which are chosen to be triangular in this work, but other element shapes can be used. The angular domain D is a sphere of directions with its center at

24 3. Methods

the origin and is sectioned in hierarchical patches D_{κ} . They are hierarchical in the sense that patches can be again divided into smaller patches. The largest patches are at level 1 and are formed by dividing the sphere into octants. The separation is created by the intersection of the sphere with the coordinate places $\Omega_x=0$, $\Omega_y=0$, and $\Omega_z=0$, creating eight spherical triangles. These triangles can be divided again into four patches at level 2. This is done by connecting the midpoints of each side of the triangle. Each level higher, the patch is divided in the same way into four sub-patches. In figure 3.1 this process is illustrated up to level 3 patches.

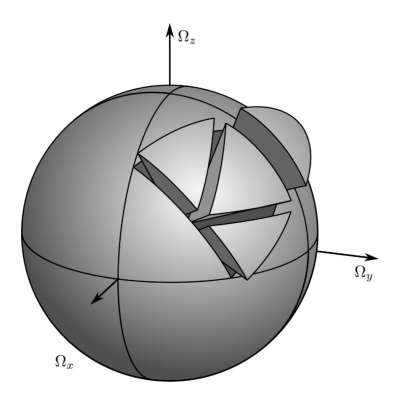


Figure 3.1: Angular domain divided hierarchically into patches. The largest triangular patches are level 1, and the subdivision of one patch into four smaller patches indicate level 2 and 3 [22].

An angular subdivision is made by defining the set of patch indices P such that all the non-overlapping patches D_p , where $p \in P$, together make up the angular domain D, i.e. $\bigcup_{p \in P} D_P = D$ and $D_p \cap D_q = \emptyset$ for $\forall p, q \in P$ where $p \neq q$. The spatial elements V_k are coupled to the angular subdivisions to create phase space elements. Within each spatial element k, the angular component of flux is described by the same set of patches at each node. However, the angular subdivision can vary between spatial elements, thereby locally refining the angular component in space.

Angular Basis Sets

To describe the angular dependence of the neutron flux within an angular patch D_k , basis functions are defined that are local to the patch.

$$\Psi_{\kappa\alpha}(\Omega) = 0 \quad \text{if} \quad \Omega \notin D_{\kappa}, \tag{3.1}$$

where $\Psi_{\kappa,\alpha}(\underline{\Omega})$ is the α th basis function of patch D_{κ} . Since basis functions are local to the patch, they can be discontinuous at the boundaries of the patch. Within the PHANTOM-DG code, the choice can be made from five sets of basis functions. In this work, only two sets are used; the *constant* set for the low-fidelity model and the *linear* set for the high-fidelity model:

Constant Every patch D_{κ} has one constant basis function; $\Psi_{\kappa,1}(\underline{\Omega})=1$ in the patch and zero outside of the patch. This is the same as the S_n method where the angular domain is divided into a discrete set of directions.

Linear The linear set is a nodal set of three basis functions that satisfy $\Psi_{\kappa,\alpha}(\underline{\Omega}_{\beta}) = \delta_{\alpha,\beta}$, where $\delta_{\alpha,\beta}$ is the Kronecker delta and $\underline{\Omega}_{\beta}$ are the corner points of the triangle patches. The standard Lagrange functions of the flat triangle are projected onto the sphere.

The constant basis function set is the simplest to compute but gives the highest absolute error of the angular flux and of the scalar flux in most cases compared to other basis function sets. These basis functions are therefore used for the low-fidelity model. The other four basis sets give comparable results regarding the absolute error of the angular and scalar flux. However, the Ω -linear scheme results

3.2. Test Case Studies 25

in significant error in the scalar flux in diffusive materials, and is, therefore, less suited for reactor calculations [22]. The description of the other three basis sets can be found in [22].

The neutron flux of equation 2.60 is approximated by summing the product of the spatial and angular basis functions over all the phase space elements

$$\phi(\underline{r},\underline{\Omega}) \approx \hat{\phi}(\underline{r},\underline{\Omega}) = \sum_{k,i} \sum_{p \in P_{k},d} \phi_{k,p}^{i,d} \Phi_{k,i}(\underline{r}) \Psi_{p,d}(\underline{\Omega}), \tag{3.2}$$

where $\Phi_{k,i}(\underline{r})$ is the ith basis functions on the spatial element k and $\Psi_{p,d}(\underline{\Omega})$ is the dth basis function of the angular element p. Following Galerkin's method, this is substituted into equation 2.60, multiplied with spatial and angular test functions $\Phi_{j,l}(\underline{r})$ and $\Psi_{q,m}(\underline{\Omega})$, respectively, and integrated over the entire phase space.

$$\int_{V} \int_{D} \Phi_{j,l}(\underline{r}) \Psi_{q,m}(\underline{\Omega}) Q(\underline{r},\underline{\Omega}) d\underline{\Omega} d\underline{r} = \sum_{\xi=1}^{3} \int_{V} \int_{D} \Phi_{j,l}(\underline{r}) \Psi_{q,m}(\underline{\Omega}) \underline{\Omega}^{\xi} \nabla_{\xi} \sum_{k,i} \sum_{p \in P_{k},d} \phi_{k,p}^{i,d} \Phi_{k,i}(\underline{r}) \Psi_{p,d}(\underline{\Omega}) d\underline{\Omega} d\underline{r}
+ \int_{V} \int_{D} \Phi_{j,l}(\underline{r}) \Psi_{q,m}(\underline{\Omega}) \Sigma_{t}(\underline{r}) \sum_{k,i} \sum_{p \in P_{k},d} \phi_{k,p}^{i,d} \Phi_{k,i}(\underline{r}) \Psi_{p,d}(\underline{\Omega}) d\underline{\Omega} d\underline{r} \quad j = 1, ..., n, q \in P_{j}, l = 1, ..., n_{j}, m = 1..., n_{a}$$
(3.3)

where $Q(\underline{r},\underline{\Omega})$ includes the source term $S((\underline{r},\underline{\Omega}))$ and the scatter term, ξ is the index of the Cartesian coordinates, n is the number of spatial elements, n_j is the number of basis functions of spatial element j, and n_a is the number of angular basis functions per angular element.

3.2. Test Case Studies

The proposed multi-fidelity ROMs methods presented in Sections 2.2.2 and 2.2.4 will be tested on three different case studies; 1D analytical functions, a 2D neutron diffusion problem, and a 2D neutron source-detector problem.

3.2.1. Case 1: 1D Analytical Models

First, the adaptation and filtering algorithms are tested on two analytical models with different multifidelity aspects for validation. For the first analytical test case, a parabola combined with a sinusoidal function is chosen of the following form

$$f(x) = Ax^2 + C \cdot \sin\left(\frac{\pi x B}{L}\right). \tag{3.4}$$

Here parameters A, B, and C will be sampled; the corresponding parameter ranges can be found in Table 3.1. The length of the domain is L=10 arb. unit. The fidelity level of the model is determined by the discretization of the spatial domain; the low-fidelity model will have a coarse grid with a step size of $h_c=0.1$ and the high-fidelity model a finer grid with a step size of $h_f=0.001$. This analytical test case will therefore be labeled as *multi-grid*. Two experiments are run, one with a greediness factor of 1 (non-greedy) and one with a factor of 0 (greedy).

Table 3.1: Parameter ranges for the high- and low-fidelity models of the multi-grid 1D analytical test case.

	Α	В	С
High-fidelity	1-5	10-15	3-5
Low-fidelity	1-5	10-15	3-5

For the *multi-physics* test case, the low-fidelity model will have only the parabola component with a dependency on parameter A:

26 3. Methods

$$f_{low}(x) = Ax^2, (3.5)$$

whereas the high-fidelity function will be again Equation 3.4, which will now be indicated as f_{high} . The presence of the sine component in the high-fidelity case represents some additional 'physical phenomenon', which is neglected in the low-fidelity case. The domain length is again L=10 arb. unit and is discretized in steps of h=0.001 for both models. The ranges for parameters A, B, and C are presented in Table 3.2. Again, a greediness factor of 0 and 1 are tested. Equations 3.4 and 3.5 are plotted for the values A=1, B=15, and C=1 to illustrate.

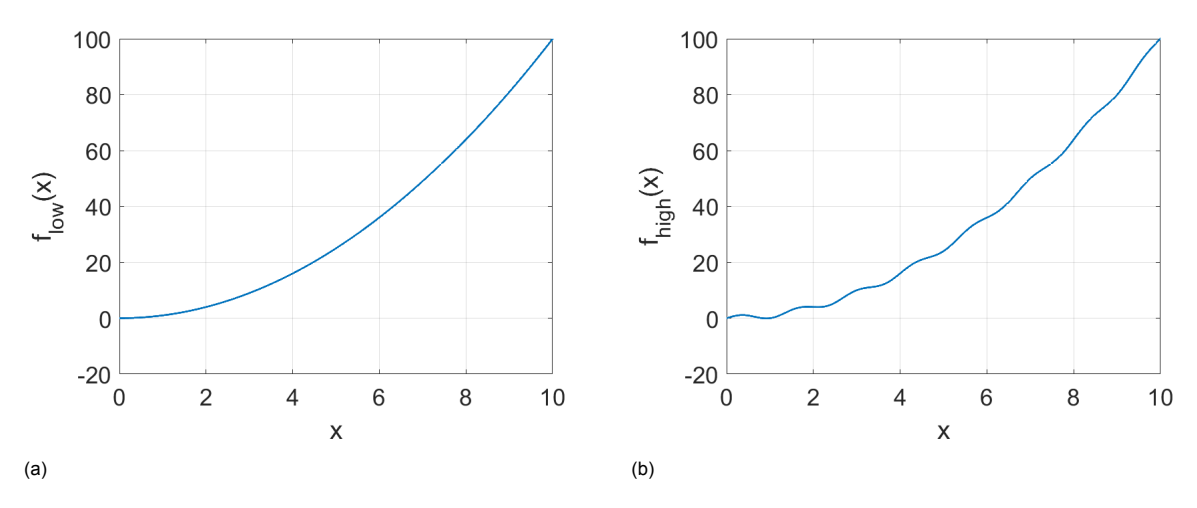


Figure 3.2: Low-fidelity (a) and high-fidelity (b) functions plotted for parameters A = 1, B = 15, and C = 1.

Table 3.2: Parameter ranges for the high- and low-fidelity models of the multi-physics 1D analytical test case.

	Α	В	С
High-fidelity	1-5	10-15	3-5
Low-fidelity	1-5	-	-

For both the multi-grid and multi-physics test case the same error thresholds are used. The local relative threshold for selecting important points is set to $\gamma_{int}=10^{-3}$ and the global error tolerance to stop the iterations is set to $\gamma_{max}=10^{-3}$. The error tolerance for truncating the POD modes is set to $\gamma_{r}=10^{-6}$ to limit the error introduced by truncation. For the adaption algorithm, the local and global error thresholds for computing the correction factor are set to $\lambda_{int}=10^{-3}$ and $\lambda_{max}=10^{-3}$.

3.2.2. Case 2: 2D One Group Neutron Diffusion

The multi-fidelity methods are tested on a 2D one-group neutron diffusion model for the second test case. The model solves a fixed source problem that is time-independent as given in equation 2.68. The geometry is fixed over time and consists a square that is 3-by-3 cm. Within this square, two regions are defined; a circular region in the middle of the square with a radius 0.6 cm indicated by R2, and the remaining area between with the central circle cut out indicated by R1. The geometry is given in figure 3.3.

3.2. Test Case Studies 27

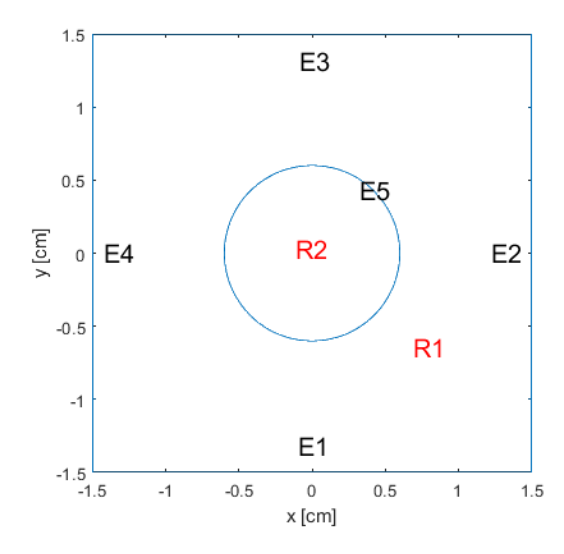


Figure 3.3: Geometry used for the 2D neutron diffusion test case. In region F1 an absorbing material is placed, while a fissile material is placed in area F2. A neutron source is placed in the circular area F2. Neumann boundary conditions are applied to all boundaries E1-E5.

In region R1 an absorber material is placed, and region R2 consists of fissile material, mimicking a fuel pin. Also, an external neutron source is placed of strength S=1. Matlab's built-in PDE solver is used to discretize the problem in space using finite elements. The high-fidelity model has a fine mesh size of $h_f=0.1$, resulting in 2016 triangular elements, while the low-fidelity model uses a mesh size of $h_c=0.5$, which gives only 130 triangular elements. The high-and low-fidelity meshes are given in figure 3.4. Furthermore, Neumann boundary conditions are applied to all boundaries E1-E5.

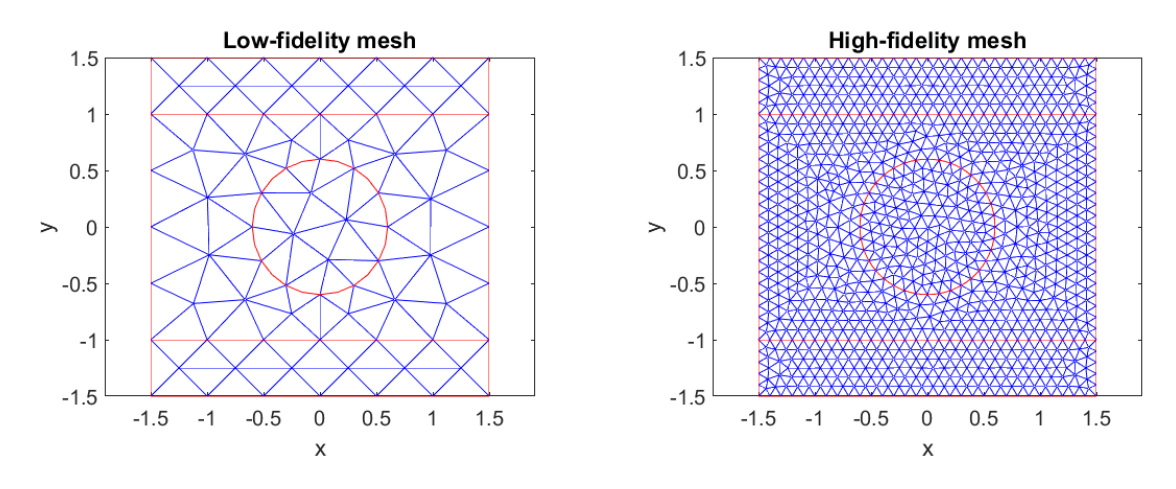


Figure 3.4: Low-fidelity and high-fidelity meshes used to solve the 2D neutron diffusion equation.

To test the multi-fidelity ROMs, three parameters will be sampled. In region R1, the diffusion coefficient D will be varied by $\pm 50\%$ of it's nominal value $D=0.759~\rm cm^2 s^{-1}$. The fission cross-section of region R2 is $\Sigma_f=0.050~\rm cm^{-1}$ and will also be varied with $\pm 50\%$.

Table 3.3: Parameters including perturbations in percentages for the two regions of the geometry used for the 2D diffusion multi-fidelity Reduced Order Models.

			Macroscopic Cross Section			
	D	S			$[cm^{-1}]$	
	$[cm^2s^{-1}]$	-	Σ_s	Σ_f	Σ_c	Σ_t
R1	0.759 ±50%	0	0.0150	Ő	$0.424 \pm 50\%$	0.439
R2	2.40	1	0.0150	$0.050 \pm 50\%$	0.074	0.139

28 3. Methods

The local relative threshold for selecting important points is set to $\gamma_{int}=10^{-3}$ and the global error tolerance to stop the iterations is set to $\gamma_{max}=10^{-3}$. The error tolerance for truncating the POD modes is set to $\gamma_r=10^{-6}$ to limit the error introduced by truncation. For the adaption algorithm, the local and global error thresholds for computing the correction factor are set to $\lambda_{int}=10^{-2}$ and $\lambda_{max}=10^{-2}$.

3.2.3. Case 3: 2D Neutron Transport

For the last test case, the time-independent one-group neutron transport equation will be solved for a fixed source problem by the Phantom-DG code. A geometry is made of a 1-by-1 cm domain with 6 areas; 4 absorbing patches (P1-P4), a neutron source (S), and the medium (M) in between. The absorbing patches are placed in the corners of the domain, where patch P1 is found in the left bottom corner, patches P2 and P3 are both in the right top corner, and patch P4 is directly above the neutron source. The patches are placed such that the neutron flux in region P1 will be independent of the absorption cross-sections of the other patches. Patch 3 will be expected to be influenced by the absorption of patch 2 since patch 2 lays on the direct line between the source and patch 3. In contrast to the other patches, patch P4 is not placed on the diagonals of the source but on it's vertical.

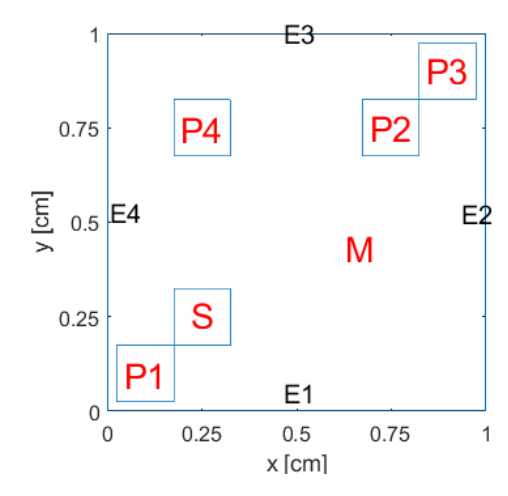


Figure 3.5: Geometry used for the 2D neutron transport test case. A source is placed in area S, and four absorbing patches indicated by P1-P4.

The geometry will be divided into triangular finite elements with characteristic length h=0.03, resulting in 2826 elements. The mesh is depicted in Figure 3.5. The angular component of the flux computed by the low-fidelity model is described by 4 patches and constant values per patch. The high-fidelity model used linear basis functions and discretized in 64 patches. A thick and a thin medium are chosen, where a thick medium has a scattering cross section of $\Sigma_s=25~{\rm cm}^{-1}$ and the thin medium $\Sigma_s=0.50~{\rm cm}^{-1}$. The parameters that will be sampled are the absorption cross-sections of regions 1-4. The parameter space ranges from $\Sigma_a=0-10~{\rm cm}^{-1}$. These cross-sections are summarized in Table 3.4 as well as the perturbations. There is no fission present in the system, so the total cross-section is $\Sigma_t=\Sigma_a+\Sigma_s$. An external neutron source of strength $S_{ext}=10$ is placed in the region S. Bare boundary conditions are applied to the edges.

3.2. Test Case Studies 29

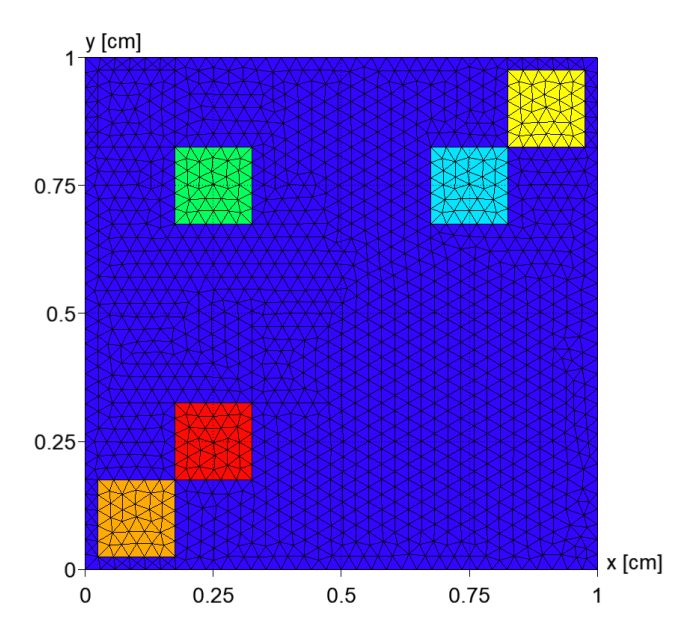


Figure 3.6: Mesh used for the 2D neutron transport test case with 2826 elements.

Table 3.4: Cross-sections for the six regions of geometry used for the 2D Neutron Transport multi-fidelity Reduced Order Model.

Region	Σα	Perturbation	Σ_S
	$\begin{bmatrix} -a \\ cm^{-1} \end{bmatrix}$		$[cm^{-1}]$
P1	5.0	±100%	0
P2	5.0	$\pm 100\%$	0
P3	5.0	$\pm 100\%$	0
P4	5.0	$\pm 100\%$	0
M	0	-	0.5, 25
S	0	-	0.5

The local relative threshold for selecting important points is set to $\gamma_{int}=10^{-3}$ and the global error tolerance to stop the iterations is set to $\gamma_{max}=10^{-3}$. The error tolerance for truncating the POD modes is set to $\gamma_r=10^{-6}$ to limit the error introduced by truncation. For the adaption algorithm, the local and global error thresholds for computing the correction factor are set to $\lambda_{int}=10^{-2}$ and $\lambda_{max}=10^{-2}$.

4

Results

?? In this section, the results of the proposed Filtered Bi-Fidelity Proper Orthogonal Decomposition method and the Adapted Bi-Fidelity Proper Orthogonal are presented and compared against the aPOD ROM of Section 2.1.3. First, the results for the analytical functions of test case 1 will be presented in Section 4.1, followed by results for the neutron diffusion model of test case 2 in Section 4.2. Finally, the results will be discussed in Section ??.

4.1. Results Case 1: 1D Analytical Functions

The proposed Filtered Bi-fidelity Proper Orthogonal and Adapted Bi-fidelity Proper Orthogonal method were tested on one-dimensional analytical functions as described in Section 3.2. The results are divided into two sections; multi-fidelity methods based on multi-grid and multi-fidelity methods based on multi-physics.

For benchmark purposes, a high-fidelity ROM (HF ROM) was built using the aPOD algorithm with a greediness factor of 1 (non-greedy) and 0 (greedy). The algorithm needed 145 snapshots to converge, of which 133 were deemed important in the non-greedy test case. Using a greediness factor of 0, the high-fidelity model sampled 301 solutions, of which again 133 points were important. The number of POD modes to build the approximation was 13 and when tested on a test set of 1000 randomly generated points, the HF ROM had a maximum relative error in the l_2 norm of $0.360 \cdot 10^{-3}$ and $0.348 \cdot 10^{-3}$ for the non-greedy and greedy algorithm respectively. Both values are below the set global tolerance of $\gamma_{max} = 10^{-3}$. These results are presented in both Tables 3.1 and 3.2.

4.1.1. Multi-grid

Table 4.1: Number of sampled points to construct the single fidelity reduced order model using a high-fidelity model (HF ROM), a low-fidelity model (LF ROM), the filtered multi-fidelity reduced order model (MF ROM), and the adapted reduced order model (MF ROM), for the 1D multigrid case. The important points are in the filtered MF ROM the important points of the high-fidelity model, while the important points for the Adapted MF ROM are for the final ROM that is constructed using corrected low-fidelity samples.

		l ou fidalitu	Liab fidality	lmmoutout	DOD Madaa	POD Modes	Maximum
Method	Greediness	Low-fidelity	High-fidelity	Important	POD Modes	Correction	relative
		snapshots	snapshots	Points	ROM	factor	error (·10 ⁻³)
HF ROM	1	-	145	133	13	-	0.360
THE ROLL	0	-	301	133	13	-	0.348
LF ROM	1	145	-	133	13	-	0.358
Li Kow	0	301	-	133	13	-	0.344
Filtered	1	145	133	133	13	-	0.360
MF ROM	0	301	133	133	13	-	0.348
Adapted	1	166	21	133	13	9	0.361
MF ROM	0	354	53	133	13	9	0.346

Filtered Multi-fidelity ROM

The FB-POD method was used to construct a filtered multi-fidelity reduced order model (filtered MF ROM) with a greediness factor of 1 (non-greedy). The number of high-fidelity evaluations or snapshots needed for this was 133, of which all were deemed important. This was as expected since the input points were already pre-selected as important by the low-fidelity run. To obtain the important points from the low-fidelity model, 145 low-fidelity snapshots had to be computed. This brings the total computational burden of the filtered MF ROM to 133 high-fidelity snapshots and 145 low-fidelity snapshots. For a non-greedy algorithm, about 8% of the number of high-fidelity evaluations is reduced by the FB-POD compared to the high-fidelity aPOD algorithm. This reduction comes at a cost of 133 extra low-fidelity snapshots. When the greediness factor is set to 0 (greedy), the reduction in high-fidelity evaluations is larger. For this greediness factor, the filtered ROM used 133 high-fidelity evaluations for this greediness factor, which reduced the number of high-fidelity evaluations by roughly 56% compared to the HF ROM. Since the greediness factor increases the number of sampled points during the pre-selection, the filtered MF ROM utilized 301 low-fidelity evaluations. The number of low- and high-fidelity snapshots used for the filtered MF ROM is presented in Table 3.1.

The filtered MF ROM, LF ROM, and HF ROM all needed the 13 POD modes to approximate the true solution and 133 important points to construct the interpolant for the coefficients of Equation 2.5, regardless of greediness. Figure 4.1 shows that the important points all share the same locations in parameter space across the ROMs, meaning that the interpolants of all ROMs is supported by the same nodes and the snapshot matrix of the HF ROM is filled with the same solutions as the MF ROM. This indicates that no information is lost in the multi-grid case by using the FB-POD algorithm compared to the high-fidelity aPOD algorithm. Furthermore, to approximate the dependence of the high-fidelity on parameters A and C, three nodes along each direction are needed. This corresponds with the linear dependence of the high-fidelity model on parameters A and C. For parameter C, 65 unique values were sampled. Furthermore, Table 4.1 shows increasing the greediness does not contribute to the construction of the reduced order model of the high-low- or multi-fidelity model in terms of the number of modes.

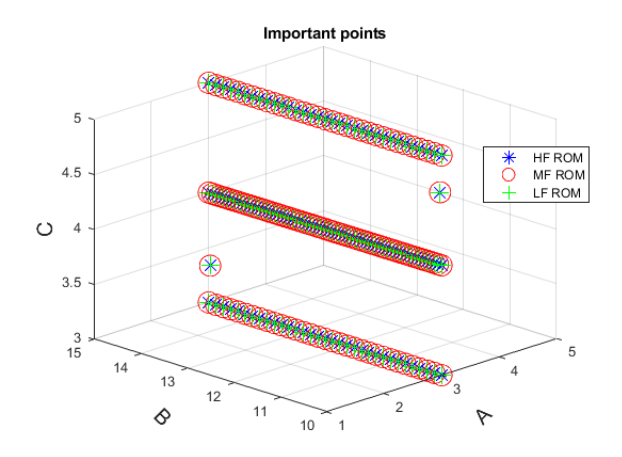
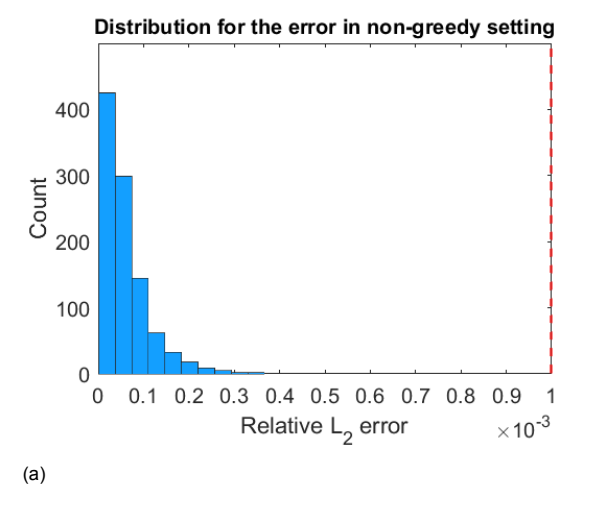


Figure 4.1: Parameter points deemed as important by the low-, high-, and filtered multi-fidelity reduced order model.

To quantify the accuracy of the filtered MF ROM, it was tested on 1000 randomly generated test points. The approximation made by the filtered MF ROM was compared against the high-fidelity solutions of the test points. The relative error for each point was calculated in the L_2 norm, given by Equation 2.29. The histogram of these errors in figure 4.2 shows that 100% of the approximations are below the given error threshold of $\gamma_{max} = 10^{-3}$ for both greediness factors. The maximum relative error was $0.360 \cdot 10^{-3}$ for the non-greedy test case and $0.348 \cdot 10^{-3}$ for the greedy test case. These values are identical for the HF ROM, since both HF ROMs and MF ROMs are constructed using the same important points and thus the same POD modes. The FB-POD algorithm, therefore in this multi-grid, yields the same reduced-order model as the aPOD algorithm in terms of accuracy and information.



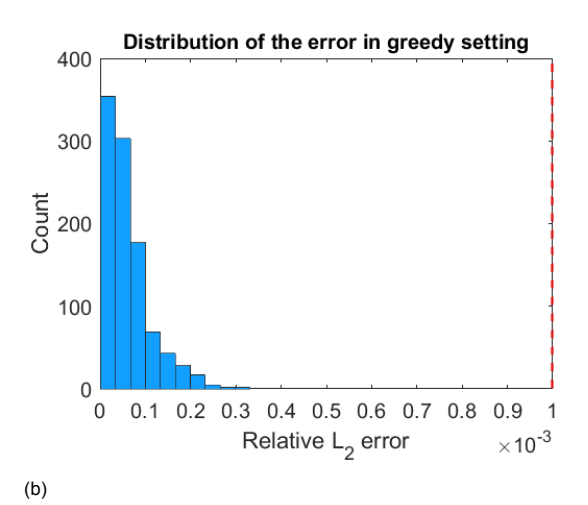


Figure 4.2: Histograms of the relative errors in the l_2 norm of the filtered Multi-Fidelity Reduced Order Model constructed the Filtered Bi-fidelity Proper Orthogonal Decomposition algorithm. A global error tolerance is set of $\gamma_{max} = 10^{-3}$. In the left image (a) a greediness factor of $\mu = 1$ is set, while the greediness factor in the right histogram (b) is set to $\mu = 0$.

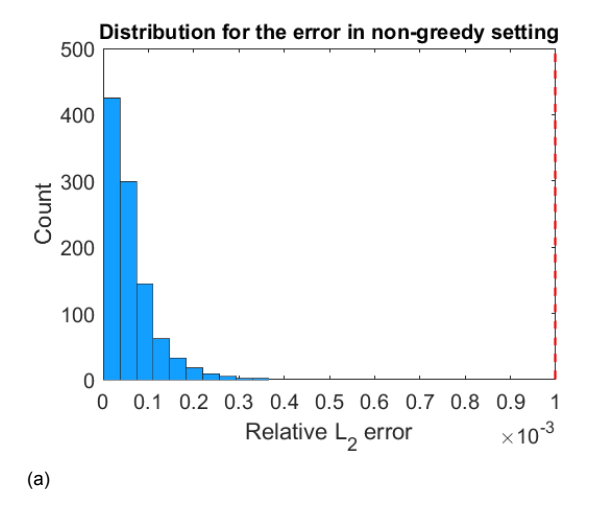
Adapted Multi-fidelity ROM

The AB-POD method was used to construct an adapted multi-fidelity reduced order model (adapted MF ROM) with a greediness factor of 1 (non-greedy). The number of high- and low-fidelity evaluations or snapshots needed to construct the additive correction C factor was 21. Furthermore, 9 POD modes are used to approximate the correction factor. This indicates that the difference between the two fidelity models is easier to learn than the solutions themselves. In addition to the high-fidelity snapshots, 145 corrected low-fidelity evaluations were needed for the AB-POD algorithm to converge, giving a total of 166 low-fidelity solutions for the construction of the adapted MF ROM. This reduced the number of high-fidelity snapshots by roughly 86% compared to the HF ROM. When the greediness factor is set to 0, 53 high- and low-fidelity points are sampled to construct the correction factor and 301 additional

low-fidelity samples were needed to construct the adapted MF ROM, bringing the total of low-fidelity evaluations to 354. Compared to the HF ROM built using the aPOD algorithm, the number of high-fidelity evaluations is reduced by 82%. The number of low- and high-fidelity snapshots used for the adapted MF ROM is presented in Table 3.1.

The adapted MF ROM ROM also needs 13 POD modes to approximate the true solution and 133 important points to construct the interpolant for the coefficients of equation 2.5. These important points are the as given in figure 4.1. This indicates that the corrected low-fidelity model snapshots are utilized in the same way as the high-fidelity snapshots during the construction of the MF ROM.

To quantify the accuracy of the adapted MF ROM, it was tested on 1000 randomly generated test points. The approximation made by the adapted MF ROM was compared against the high-fidelity solutions of the test points. The relative error for each point was calculated. The histogram of these errors in Figure 4.3 shows that 100% of the approximations are below the given error threshold of $\gamma_{max}=10^{-3}$ for both greediness factors. The maximum relative error was $0.361 \cdot 10^{-3}$ for the non-greedy test case and $0.346 \cdot 10^{-3}$ for the greedy test case. These values are comparable to the HF ROM. The AB-POD algorithm in this multi-grid case yields the same reduced-order model as the aPOD algorithm in terms of accuracy and information.



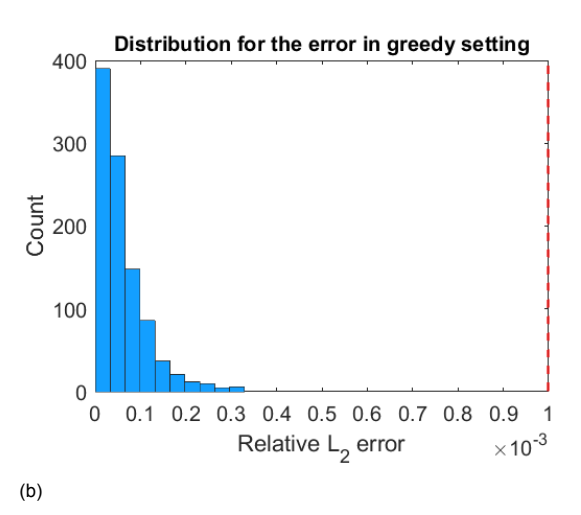


Figure 4.3: Histograms of the relative errors in the l_2 norm of the adapted Multi-Fidelity Reduced Order Model constructed by the Adapted Bi-fidelity Proper Orthogonal Decomposition algorithm. A global error tolerance is set of $\gamma_{max} = 10^{-3}$. In the left image (a) a greediness factor of $\mu = 1$ is set, while the greediness factor in the right histogram (b) is set to $\mu = 0$.

4.1.2. Multi-physics

Table 4.2: Number of sampled points to construct the single fidelity reduced order model using a high-fidelity model (HF ROM), a low-fidelity model (LF ROM), the filtered multi-fidelity reduced order model (MF ROM), and the adapted reduced order model (MF ROM), for the 1D multiphysics case. The important points are in the filtered MF ROM the important points of the high-fidelity model, while the important points for the Adapted MF ROM are for the final ROM that is constructed using corrected low-fidelity samples.

		1 £ .l . 124	11:-b & d-11:-		POD Modes	POD Modes	Maximum
Method	Greediness	Low-fidelity	High-fidelity	Important		Correction	relative
		snapshots	snapshots	Points	ROM	factor	error ($\cdot 10^{-3}$)
HF ROM	1	-	145	133	13	-	$0.360 \cdot 10^{-3}$
HF KOW	0	-	301	133	13	-	$0.348 \cdot 10^{-3}$
LF ROM	1	9	-	3	1	-	$4.06 \cdot 10^{-14}$
LI KOM	0	17	-	3	1		- 4.28 · 10 ⁻¹⁴
Filtered	1	9	3	3	1	-	0.095
MF ROM	0	17	3	3	1	-	0.099
Adapted	1	1176	1031	133	13	14	$0.372 \cdot 10^{-3}$
MF ROM	0	2616	2315	133	13	14	$0.356 \cdot 10^{-3}$

Filtered Multi-fidelity ROM

For the test case involving multiple physics, the FB-POD algorithm was used to build a filtered MF ROM with both a greedy and non-greedy algorithm. The FB-POD algorithm utilized the low-fidelity model, which is a parabolic function dependent solely on parameter A, to pre-select points. From the 9 sampled points, only 3 were deemed important in the non-greedy case, the root node and the two forward points. This reduces the number of high-fidelity snapshot by 98% compared to the high-fidelity aPOD ROM. One POD mode sufficed for describing the low-fidelity model. Constructing a MF ROM using three high-fidelity snapshots resulted in a maximum error of 0.095. Furthermore, the histogram of Figure 4.5 (a) indicates that out of the 1000 tested points, 998 exceeded the predefined global threshold of $\gamma_{int}=10^{-3}$. To illustrate the inadequacy of the filtered MF-ROM, a randomly sampled test point (3, 14, 3) is depicted for the low-, high-, and multi-fidelity ROMs. The multi-fidelity solution adheres to the dominant curve of the parabola but diverges from the sine component of the high-fidelity function. Setting the greediness factor to 0 yields 17 sampled points, with the same 3 values being deemed as important. Figure 4.5 (b) shows that a 996 points exceeded the relative tolerance of 10^{-3} for the greedy algorithm, and yielded a maximum relative error of 0.099.

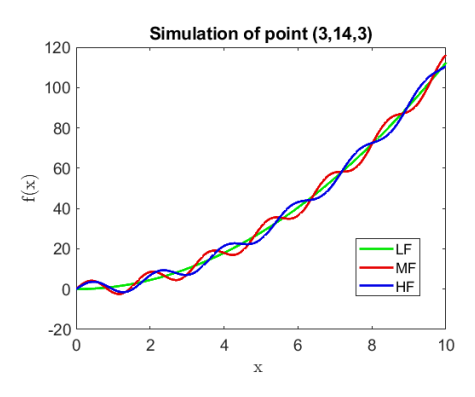


Figure 4.4: Approximation by the high-fidelity ROM (blue) and multi-fidelity ROM (red) of $f_{high} = 3x^2 + 3 \cdot sin(\frac{14\pi x}{10})$ are plotted. Also, the approximation by the low-fidelity ROM (green) of $f_{low} = 3x^2$ is given.

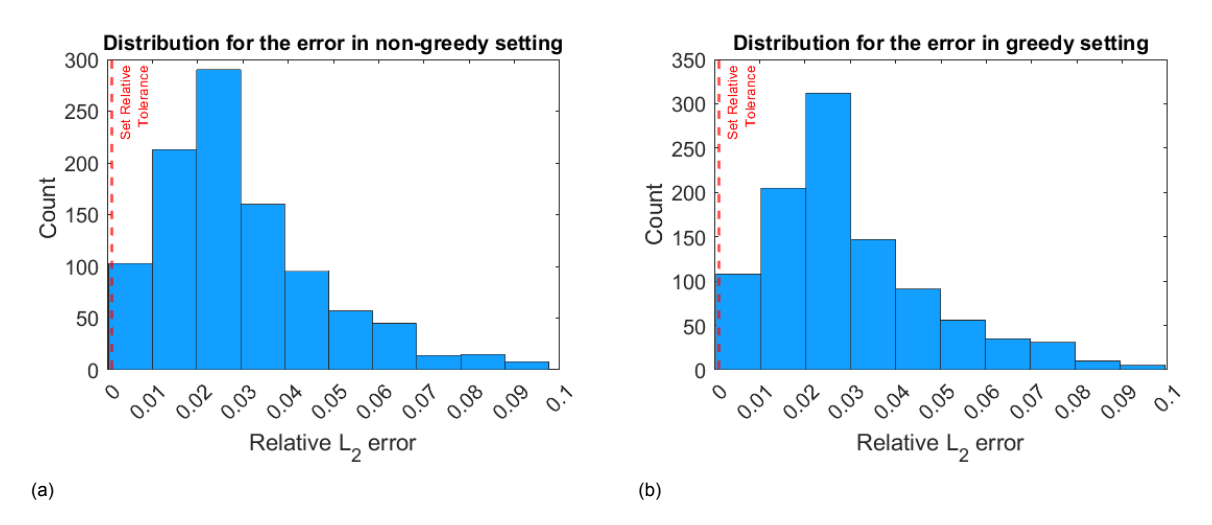


Figure 4.5: Histograms of the relative errors in the l_2 norm of the filtered Multi-Fidelity Reduced Order Model constructed the Filtered Bi-fidelity Proper Orthogonal Decomposition algorithm. A global error tolerance is set of $\gamma_{max} = 10^{-3}$. In the left image (a) a greediness factor of $\mu = 1$ is set, while the greediness factor in the right histogram (b) is set to $\mu = 0$.

Adapted Multi-fidelity ROM

The AB-POD method was used to construct an adapted multi-fidelity reduced order model (adapted MF ROM) with a greediness factor of 1 (non-greedy) based on the 1D analytical multi-physics functions. The number of high- and low-fidelity evaluations or snapshots needed to construct the additive correction factor was 1031. This is an increase of 611% in the number of high-fidelity evaluations needed compared to high-fidelity ROM. The correction factor was approximated by 14 POD modes. In addition, the number of corrected low-fidelity snapshots needed to converge the FB-POD algorithm was 145, giving a total of 1176 low-fidelity solutions for the construction of the adapted MF ROM. When the greediness factor is set to 0, 2315 high- and low-fidelity points are sampled to construct the correction factor and 301 additional low-fidelity samples were needed to construct the adapted MF ROM, bringing the total of low-fidelity evaluations to 2616. In the greedy setting, the number of high-fidelity evaluations is increased by 669% by the adapted MF ROM. For both the non-greedy and greedy algorithm, the final adapted MF ROM utilized 13 POD modes to construct approximations in the online phase. The number of low- and high-fidelity snapshots used for the adapted MF ROM is presented in Table 3.1.

To analyze the behavior of the adapted MF ROM, the square singular values of the POD modes used to approximate the high-fidelity model by the high-fidelity aPOD ROM is shown in Figure 4.6a. The square of the singular value is a measure of how much energy is contained in the corresponding mode. Figure 4.6b shows the corresponding 13 POD modes. The first mode is dominant in approximating the high-fidelity solution, as the square of the first singular value is 10^4 times larger than the second to largest singular value.

In Figure 4.7a, the square of the singular values of the POD modes that are used to construct the correction factor of the AB-POD algorithm are shown. The corresponding 14 POD modes are depicted in Figure 4.7b. The dominant POD mode of Figure 4.6b is absent in the spectrum of Figure 4.7b.

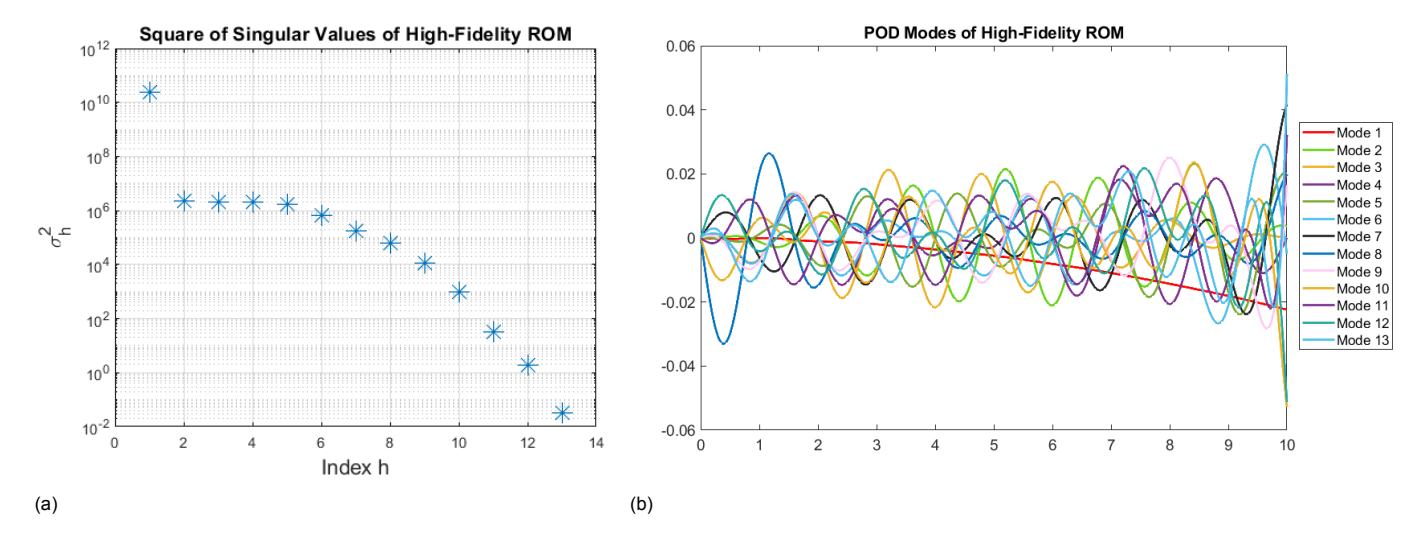


Figure 4.6: Square of singular values for the 13 POD modes used to approximate the high-fidelity model by the HF ROM (a) and the corresponding 13 POD modes used to approximate the high-fidelity model by the HF ROM (b).

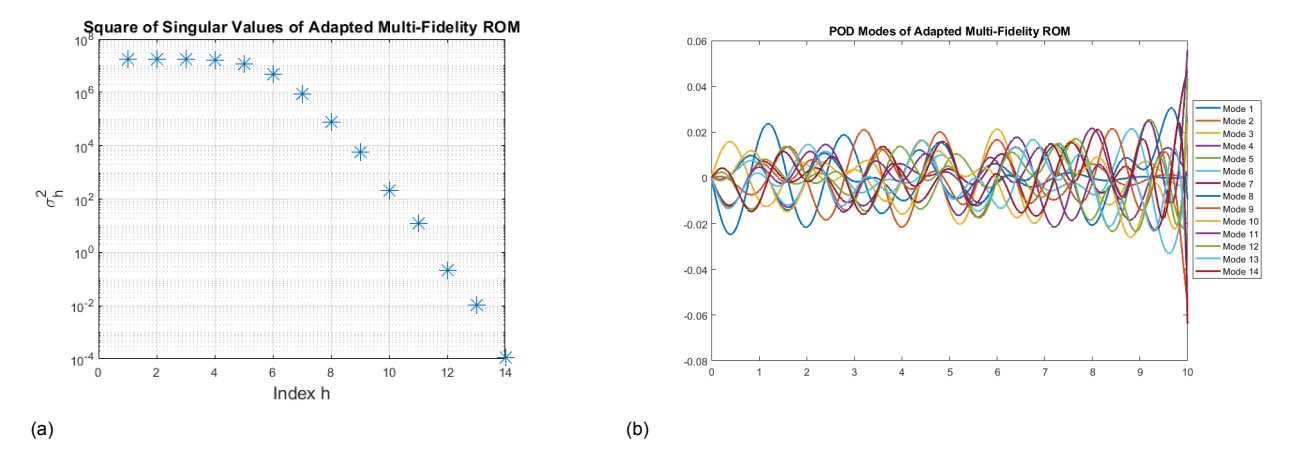


Figure 4.7: Square of singular values for the 14 POD modes used to approximate the correction factor by the adapted MF ROM (a) and the corresponding 14 POD modes (b).

The global relative error tolerance for the correction factor λ_{max} can be set independently of the global error threshold for the final multi-fidelity ROM γ_{max} . The threshold λ_{int} is relaxed to reduce the number of points needed for the correction factor ${\bf C}$ for the adapted multi-fidelity ROM. Table 4.3 shows the number of high-fidelity snapshots needed to construct the adapted multi-fidelity ROM for different values of λ_{int} , using a non-greedy algorithm. The multi-fidelity ROMs with less stringent error thresholds are then tested using 1000 random test points. Table 4.3 also provides the maximum relative error observed when testing the multi-fidelity ROM on these points and the number of points that fall below the predetermined global threshold γ_{int} . Figure 4.8 shows the histograms of the relative errors when testing the multi-fidelity ROM for error tolerances ranging from $10^{-1}-10^{-4}$. From the 1000 test points, 988 still fall under the set global tolerance of γ_{max} when a relaxed correction error tolerance was used of $\lambda_{max}=10^{-1}$. To construct the correction factor, 71 high-fidelity snapshots were used. This is a reduction of 51% compared to the high-fidelity ROM.

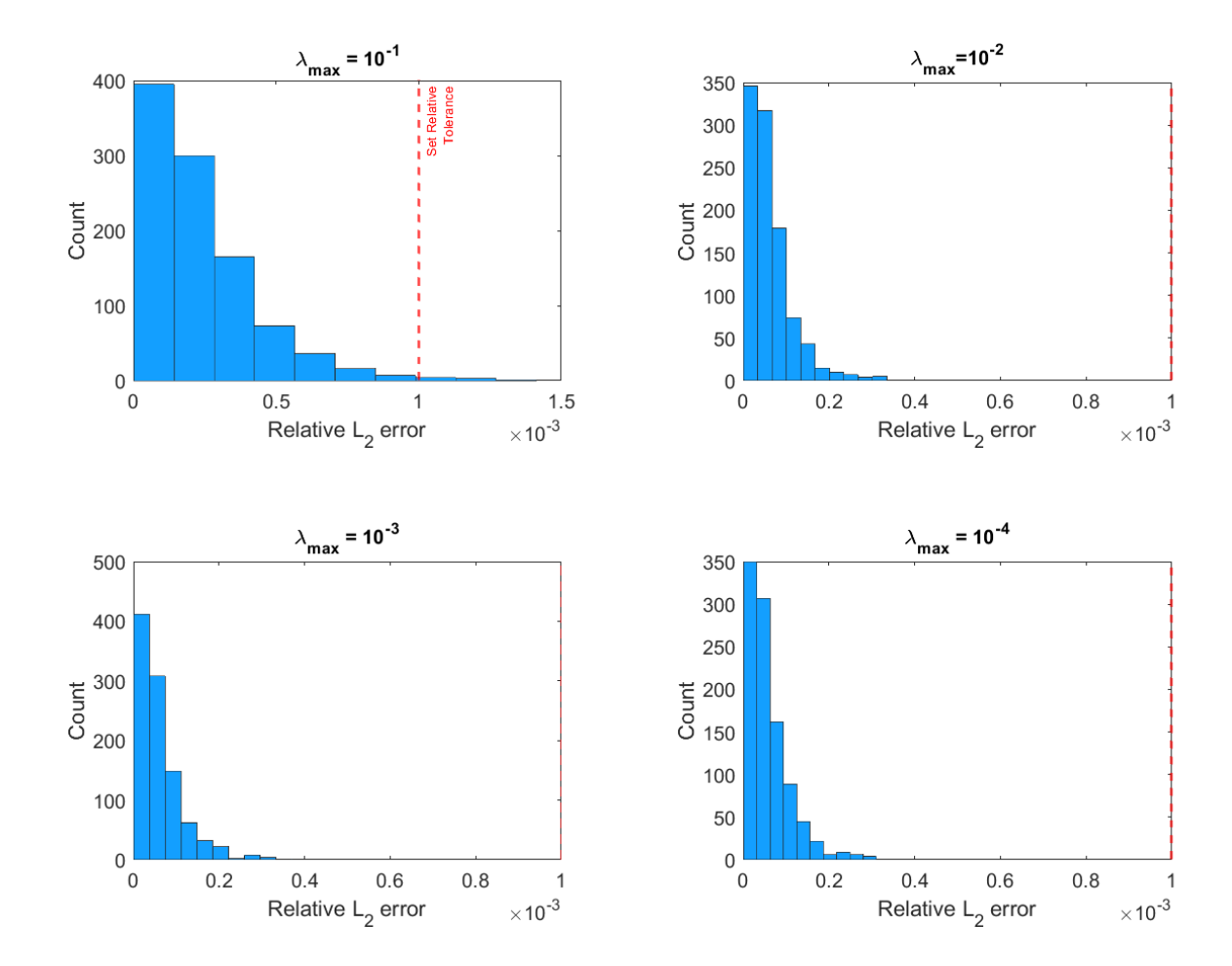


Figure 4.8: Histograms of the relative errors in the l_2 norm of the adapted Multi-Fidelity Reduced Order Model (MF ROM) constructed by the Filtered Bi-fidelity Proper Orthogonal Decomposition method using a non-greedy algorithm. Four global error tolerances for the additive correction factor are set ranging from $\lambda max = 10^{-4} - 10^{-1}$. The overall global relative error tolerance for the MF ROM is set to $\gamma_{max} = 10^{-3}$.

Table 4.3: Histograms of the relative errors in the l_2 norm of the adapted Multi-Fidelity Reduced Order Model for different values of global relative error tolerance λ_{max} for approximating the correction factor.

Relative error tolerance C λ_{max}	High-fidelity snapshots	Max. relative error (·10 ⁻³)	% approximations below global threshold
10^{-4}	2055	0.315	100%
10^{-3}	1031	0.335	100%
10^{-2}	263	0.334	100%
10^{-1}	71	1.24	98.8%

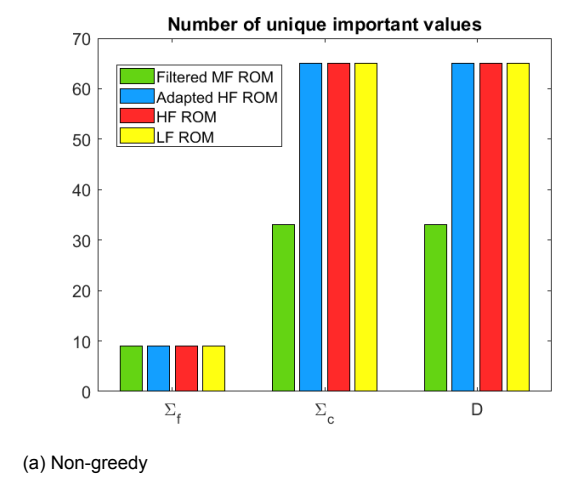
4.2. Results Case 2: 2D Neutron Diffusion

The proposed Filtered Bifidelity Proper Orthogonal and Adapted Bifidelity Proper Orthogonal method were tested on a two-dimensional neutron diffusion model, solving Equation 2.68 of Section 2.3.2. The variable fidelity between the two models was based on different discretization of the mesh. A high-fidelity ROM (HF ROM) was built using the aPOD algorithm with the mesh size of $h_f=0.1$ for comparison. The HF ROM was constructed with a greediness factor of 1 (non-greedy) and 0 (greedy). 677 points were sampled of which 535 were deemed important in the non-greedy test case. Using a greediness factor of 0, the high-fidelity model sampled 871 solutions, of which 562 points were important. The number of POD modes to build the approximation was 5 in the non-greedy setting, and

7 in the greedy setting. When tested on a test set of 1000 randomly generated points, the HF ROM had a maximum relative error $0.324 \cdot 10^{-3}$ and $0.309 \cdot 10^{-3}$ in the l_2 norm of non-greedy and greedy algorithm respectively. Both values are below the set global tolerance of $\gamma_{max} = 10^{-3}$. These results are presented in both Table 4.4.

Table 4.4: Number of sampled points to construct the single fidelity reduced order model using a high-fidelity model (HF ROM), a low-fidelity model (LF ROM), the filtered multi-fidelity reduced order model (MF ROM), and the adapted reduced order model (MF ROM), for the 2D neutron diffusion model. The important points are in the filtered MF ROM the important points of the high-fidelity model, while the important points for the Adapted MF ROM are for the final ROM that is constructed using corrected low-fidelity samples.

		l our fidality	Lliab fidality	lmmoutout	DOD Madas	POD Modes	Maximum
Method	Greediness	Low-fidelity	High-fidelity	Important	POD Modes	Correction	relative
		snapshots	snapshots	Points	ROM	factor	error (·10 ⁻³)
HF ROM	1	-	677	535	5	-	0.324
TII KOW	0	-	871	562	7	-	0.309
LF ROM	1	675	-	537	5	-	0.323
LF ROW —	0	872	-	564	5	-	0.328
Filtered	1	675	317	317	5	-	1.20
MF ROM	0	872	327	327	5	-	1.08
Adapted	1	1034	357	543	7	3	0.372
MF ROM	0	1276	401	567	7	3	0.345



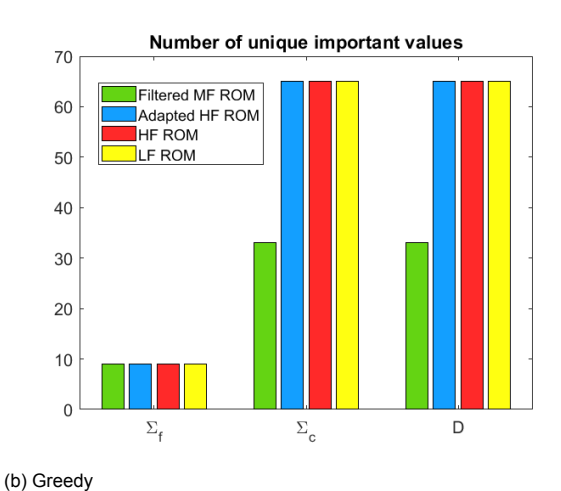


Figure 4.9: Histograms of the unique values sampled for each parameter by the filtered MF ROM, adapted MF ROM, HF ROM and LF ROM, using a non-greedy (a) and greedy (b) algorithm.

Filtered Multi-Fidelity ROM

The FB-POD method was used to construct a filtered multi-fidelity reduced order model with a greed-iness factor of 0 and 1. The low-fidelity model sampled 675 points, of which 537 were identified as important in the non-greedy setting. These points were transferred to the high-fidelity part of FB-POD algorithm. The FB-POD however converged already after 317 high-fidelity snapshots. This means that the filtered MF ROM could already predict the forward points with an accuracy below 10^{-3} . This

reduced the number of high-fidelity samples by 53% compared to the high-fidelity aPOD ROM. 5 POD modes were used to construct the approximations by the MF ROM. In the greedy setting, the low-fidelity sparse grid search sampled 872 points, of which 564 were deemed as important. When transferred to the high-fidelity section, 327 were utilized to build the MF ROM. This reduced the number of high-fidelity evaluations by 62% compaired to the HF ROM. The number of low- and high-fidelity snapshots used for the filtered MF ROM is presented in Table 4.4. To illustrate the filtered MF ROM, Figure 4.10a shows the true solution for the neutron flux for a randomly sampled point with parameters $\Sigma_f = 0.049~{\rm cm}^{-1}, \Sigma_c = 0.31~{\rm cm}^{-1},$ and $D = 0.84~{\rm cm}^2 {\rm s}^{-1}$ and Figure 4.10b shows the approximation for that same parameter points made by the non-greedy filtered multi-fidelity ROM.

Figure 4.9 shows the number of uniquely sampled values per parameter for each the high-, low-, and multi-fidelity ROMs. The FB-POD algorithm sampled fewer values for the macroscopic cross-section and diffusion coefficient compaired to the other ROMs.

When tested on 1000 randomly sampled points, the non-greedy FB-POD had a maximum relative error of $1.08 \cdot 10^{-3}$ and the greedy FB-POD $1.20 \cdot 10^{-3}$, both values are below the set relative tolerance of 10^{-3} . Figure 4.11 shows the histograms of the relative errors of the 1000 generated test points. In the greedy setting 99.5% of the tested points were still below the set relative tolerance, while in the non-greedy setting 98.9% of the sampled point fell still within allowed limits.

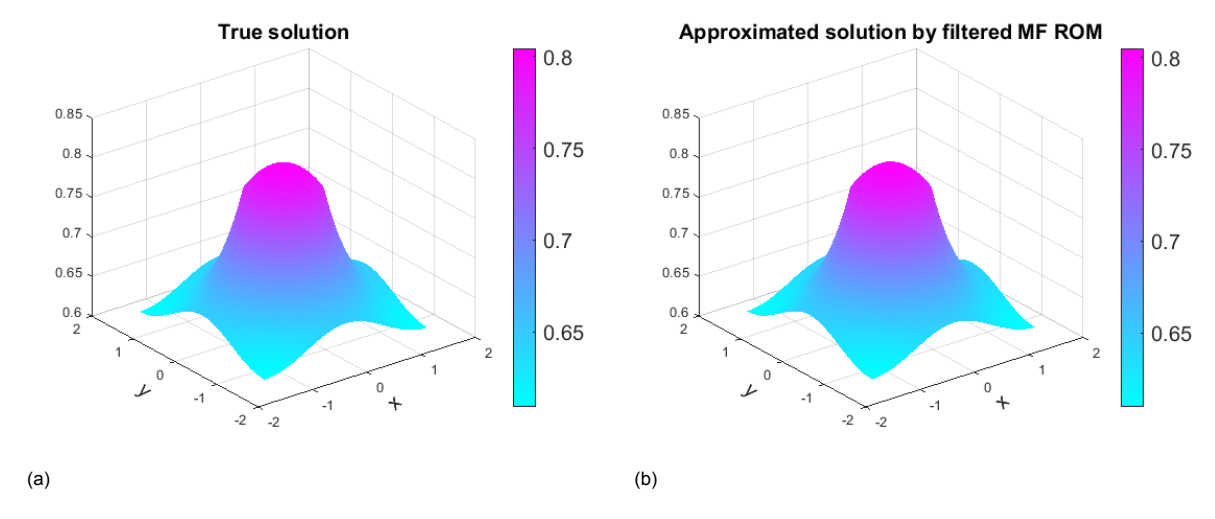
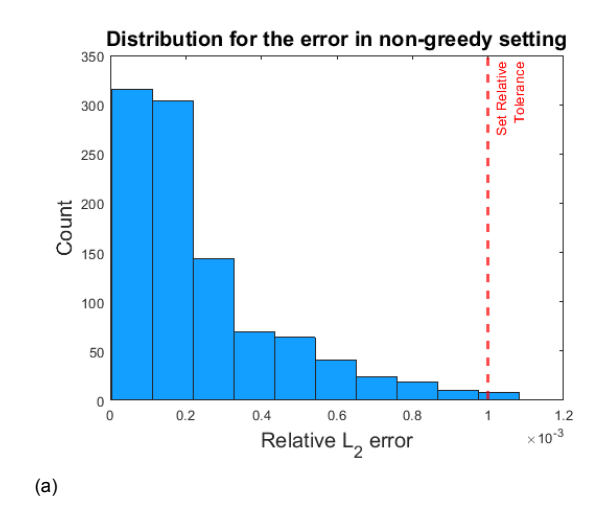


Figure 4.10: The true solution for the neutron flux of Section 3.2 computed by Matlab's in-built PDE solver using the high-fidelity mesh for a randomly sampled point (a) and the approximation of this solution made by the filtered multi-fidelity ROM (b). The parameters of the point are $\Sigma_f = 0.049 \, \mathrm{cm}^{-1}$, $\Sigma_c = 0.31 \, \mathrm{cm}^{-1}$, and $D = 0.84 \, \mathrm{cm}^2 \mathrm{s}^{-1}$.



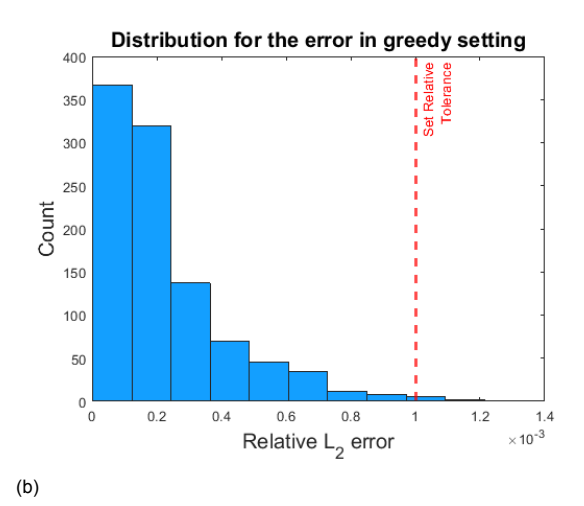


Figure 4.11: Histograms of the relative errors in the l_2 norm of the adapted Multi-Fidelity Reduced Order Model constructed by the Filtered Bi-fidelity Proper Orthogonal Decomposition algorithm. The MF ROMs are built based on a 2D diffusion problem. A global error tolerance is set of $\gamma_{max}=10^{-3}$. In the left image (a) a greediness factor of $\mu=1$ is set, while the greediness factor in the right histogram (b) is set to $\mu=0$.

Adapted Multi-Fidelity ROM

The AB-POD method was used to construct an adapted multi-fidelity reduced order model based on the 2D neutron diffusion model. The method was used using a greedy and non-greedy algorithm. The number of high- and low-fidelity evaluations or snapshots needed to construct the additive correction factor was 357. This reduces the number of high-fidelity samples by 47% The correction factor was approximated by 3 POD modes. In addition, the number of corrected low-fidelity snapshots needed to converge the AB-POD algorithm was 677, giving a total of 1034 low-fidelity solutions for the construction of the adapted MF ROM. When the greediness factor is set to 0, high- and low-fidelity 401 points are sampled to construct the correction factor and 1276 additional low-fidelity samples were needed to construct the adapted MF ROM, bringing the total of low-fidelity evaluations to 1677. The number of high-fidelity solutions was reduced by 54% compared to the high-fidelity aPOD method. The correction factor was again approximated by 3 POD modes. The adapted MF ROM in both greediness settings 5 POD modes to approximate high-fidelity solutions in the online phase. The number of lowand high-fidelity snapshots en POD modes used for the adapted MF ROM is presented in Table 4.4. Figure 4.12a shows the true solution for the neutron flux for a randomly sampled point with parameters $\Sigma_f=0.035~{
m cm^{-1}}, \Sigma_c=0.40~{
m cm^{-1}},$ and $D=0.40~{
m cm^2s^{-1}}$ and Figure 4.12b shows the approximation for that same parameter points made by the adapted multi-fidelity ROM.

In Figure 4.9, it can be seen that the AB-POD algorithm samples the same number of unique values per dimension as the high-fidelity model. This indicates that the corrected low-fidelity snapshots contains similar information as the high-fidelity snapshots.

The global error tolerance to stop iterations for the correction factor was set to $\lambda_{max}=10^{-2}$, while the global error tolerance that was used for the final multi-fidelity ROM was kept on $\gamma_{max}=10^{-3}$. Section 3.2.1 revealed that a less accurate approximation to the correction factor still yields an accurate final multi-fidelity ROM with a lower cost of high-fidelity snapshots. Consequently, the threshold λ_{int} was reduced and resulted indeed in a reduction of high-fidelity snapshots.

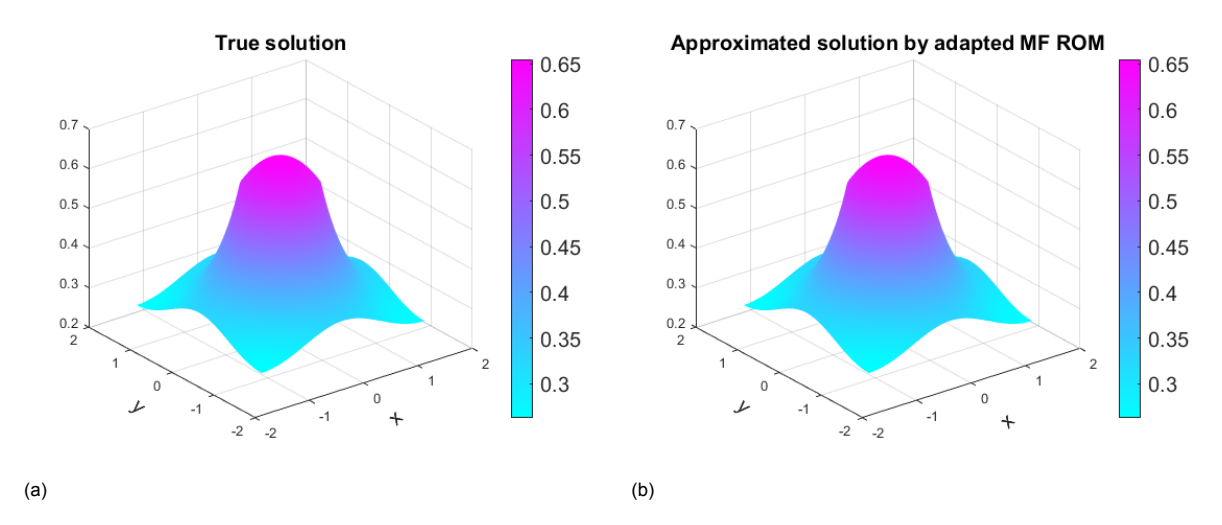


Figure 4.12: The true solution for the neutron flux of Section 3.2 computed by Matlab's in-built PDE solver using the high-fidelity mesh for a randomly sampled point (a) and the approximation of this solution made by the adapted multi-fidelity ROM (b). The parameters of the point are $\Sigma_f = 0.035 \text{ cm}^{-1}$, $\Sigma_c = 0.40 \text{ cm}^{-1}$, and $D = 0.40 \text{ cm}^2 \text{s}^{-1}$.

When tested on 1000 randomly sampled test points, the non-greedy AB-POD generated ROM yielded a maximum error of $0.372 \cdot 10^{-3}$ in the l_2 norm, while the greedy version yielded a maximum error of $0.345 \cdot 10^{-3}$. Figure 4.13 shows the histograms of the relative errors of the 1000 generated test points. Though the correction factor had a looser error threshold compared to the final multi-fidelity ROM, all samples that were tested fell under the preset global error threshold of $\gamma_{max} = 10^{-3}$.

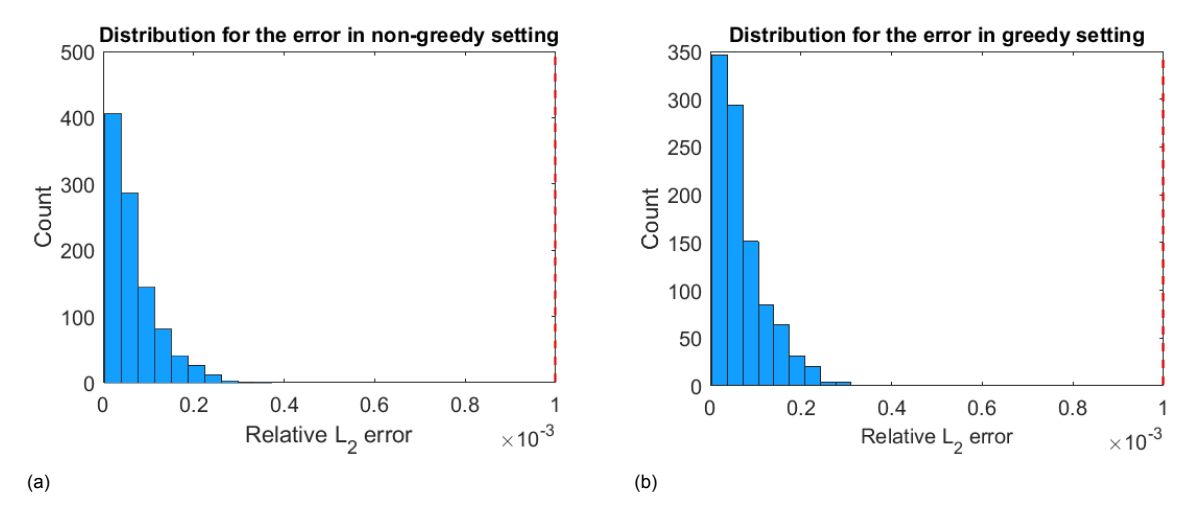
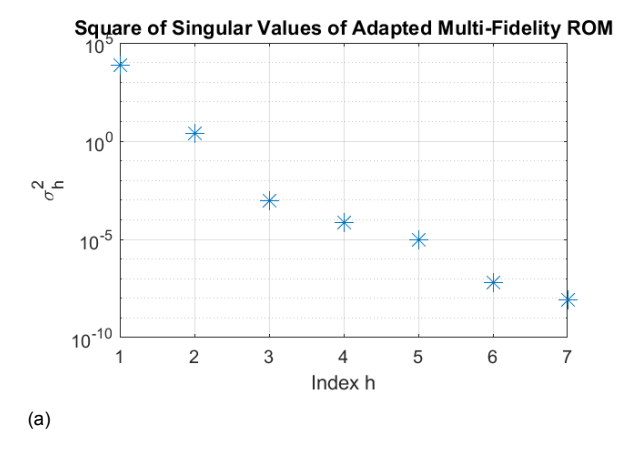


Figure 4.13: Histograms of the relative errors in the l_2 norm of the adapted Multi-Fidelity Reduced Order Model constructed by the Adapted Bi-fidelity Proper Orthogonal Decomposition algorithm. The MF ROMs are built based of a 2D diffusion problem. A global error tolerance is set of $\gamma_{max}=10^{-3}$. In the left image (a) a greediness factor of $\mu=1$ is set, while the greediness factor in the right histogram (b) is set to $\mu=0$.

Notably, 7 POD modes were used for the adapted MF ROM, while the LF ROM used 5 POD modes in both greediness settings and the HF ROM in the non-greedy setting. In Figure 4.14, the square of the singular values for the corresponding POD modes of the adapted MF ROM are given, as well as those of the high-fidelity ROM in the non-greedy setting for comparision.



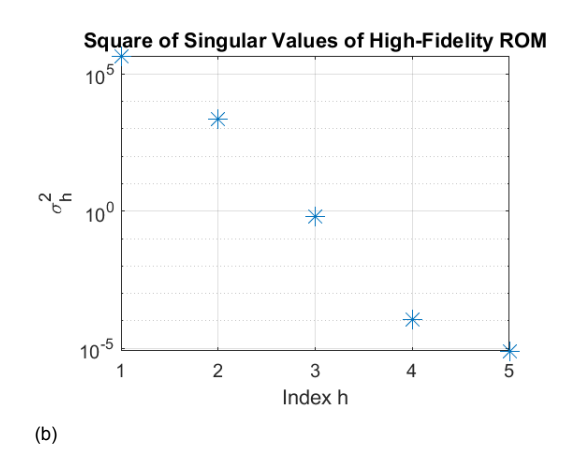
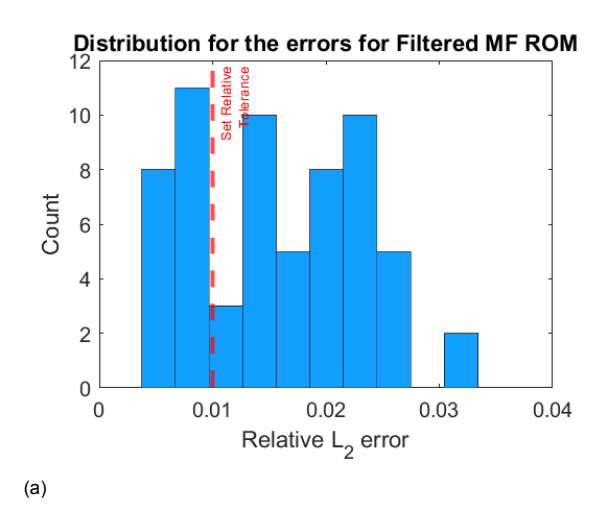


Figure 4.14: Singular values squared for the 7 POD modes used by the adapted MF ROM (a) and the 5 POD modes used for the single-fidelity HF ROM for the non-greedy algorithm (b).

4.3. Case study 3: 2D Neutron Transport

Due to technical problems, only a filtered MF ROM was constructed using a non-greedy algorithm for the 2D Neutron Transport equation in a thin material. The relative global error tolerance for the low-fidelity grid search was set to $\zeta_{max}=0.010$. The low-fidelity grid search sampled 75 points, of which 42 were deemed as important. These were transferred to the high-fidelity part, all 42 points were used to construct the filtered MF ROM. The filtered MF ROM was tested on a randomly generated test set of 65 points and yielded a maximum relative error of 0.0332. Furthermore, 43 out of the 65 tested points were above the error tolerance of 0.010. Due to technical difficulties and time constraints, a larger test set could not be obtained.

For benchmark purposes, an HF ROM was constructed using the aPOD algorithm for the thin material with global error tolerance of $\gamma_{max}=0.010$. Of the 65 high-fidelity snapshots that were sampled, 42 were deemed important. When tested on the 65 test points, the maximum relative error was 0.0332, which exceeds the set global error tolerance. Furthermore, 65% of the tested points exceeded this error tolerance. As the algorithm is designed to converge after the ROM can approximate the high-fidelity solution with an accuracy of 0.010, these results cannot be deemed as reliable. It is not clear if the construction of the HF ROM or the construction of the test set was insufficient. Furthermore, a test set of 65 points is not large enough to accurately test the HF ROM and filtered MF ROM. Figure 4.15, show the histograms for the relative errors of the 65 tested points.



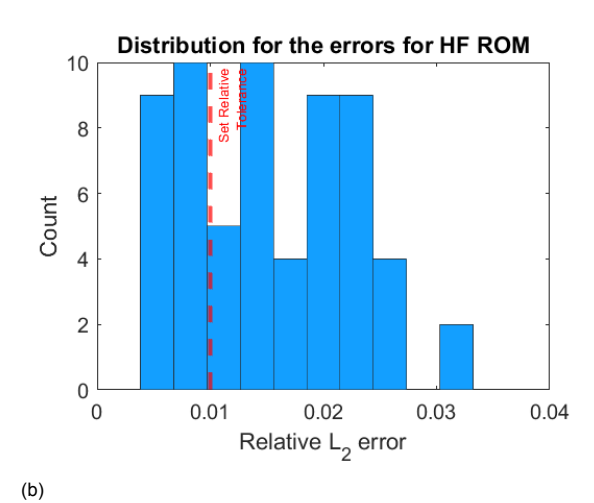


Figure 4.15: Histograms of the relative errors in the l_2 norm of the adapted Multi-Fidelity Reduced Order Model constructed by the Filtered Bi-fidelity Proper Orthogonal Decomposition algorithm (a), and of the single-fidelity aPOD MOD based on a high-fidelity model. A global error tolerance is set of $\gamma_{max} = 10^{-2}$.

This concluded the Results section of this thesis. In the next section, these results will be discussed for each of the FB-POd and AB-POD algorithms.

Discussion

In this section, the results of Section 4 will be discussed. The discussion is split into two parts: first, the results for the Filtered Bi-Fidelity Proper Orthogonal Decomposition method are discussed in Section 5.1. Then, the methods to assess the FB-POD are evaluated. The meaning of these results in an academic context is also mentioned. Secondly, the results of the Adapted Bi-Fidelity Proper Orthogonal Decomposition are discussed in Section 5.2. The evaluation methods and the academic relevance of the AB-POD algorithm are discussed as well.

5.1. Filtered Bi-Fidelity Proper Orthogonal Decomposition

In this work the FB-POD algorithm was demonstrated on 1D analytical functions for multi-grid and multi-physics variable fidelity, and on a 2D diffusion model. Both test cases showed that when the multi-fidelity approach relied on multi-grid, 8-56% of the high-fidelity snapshot could be reduced in the 1D analytical case and 53-62% in the 2D diffusion case compared to the high-fidelity aPOD algorithm. Tables 3.1 and 4.2 show that a greedy algorithm increased the number of low-fidelity snapshots significantly during the grid search. These extra sampled points did not increase the number of POD modes used in both of the cases, nor did they significantly increase the number of important points. In the 1D test case, the number of important points was the same for both greediness factors, while the number of important points in the 2D test case only increased by 3% between greediness factors. Therefore the maximum relative errors of the filtered MF ROMs did not improve significantly by using a greedy algorithm. In these test cases, the greedy algorithm mostly induced oversampling during the grid search. This can be explained by the fact that the dependence along some dimensions is linearly or close to linear, and refining the grid along those dimensions is not necessary, as the dependence can already be approximated accurately with a few supporting nodes. This is in agreement with the results found in [2] where setting the greediness factor from 1 to 0 led to a large increase in sampled points with a limited increase in accuracy. In this work, only two greediness factors were used for the prove of concept of the FB-POD algorithm. Since the greediness factor has a significant effect on the oversampling by the low-fidelity search, and thus on the reduction of high-fidelity snapshots, other values between 0-1 can be tested in further research.

Due to the similarity of both fidelity models using multi-grid, the low-fidelity adaptive grid search selected the same important points for the high-fidelity part of the FB-POD algorithm. In the 1D analytical test case, these important points were identical because both models depend on the same parameters and treat them the same way. Therefore, the snapshot matrices of both reduced-order models were filled with the same snapshots, and their proper orthogonal decomposition basis function sets were identical. Consequently, the maximum relative error of the filtered MF ROM was identical to that of the HF ROM. However, there was variance in the maximum relative error between different greediness factors even though the same important points were used. This could be explained by the fact that the HF and filtered MF ROM were tested on different randomly sampled test sets. Since the test sets are randomly generated, the maximum relative error can vary between sets. Nevertheless, the values for the non-greedy and greedy filtered MF ROM were comparable. The reason for examining the maximum

46 5. Discussion

mum relative error rather than the average error for the 1000 test points is that the reduced-order model is constructed to compute approximations below a specific error tolerance. To test if the construction was successful, the reduced-order model is evaluated for many input points to ensure convergence over the whole phase space, which was the case for the 1D multi-grid test case.

In contrast to the 2D test case, the maximum relative error in the non-greedy case was 0.095, while it was 0.099 in the greedy case. This exceeded the set error tolerance of 10⁻³. The reduced accuracy can be explained by the fact that not all preselected points were utilized by the FB-POD algorithm in the 2D diffusion test case. The FB-POD algorithm utilized only 317 of the 537 selected important points in the non-greedy setting, and 327 out of 564 in the greedy case. This can be explained by how the FB-POD algorithm is constructed. To limit the number of high-fidelity evaluations by FB-POD algorithm. the filtered MF ROM was tested after each level of important points was fed. The test points were the important points of the next level. These points were chosen as the test points because their highfidelity solutions are needed for building the interpolant at the next level. If randomly sampled points were chosen to evaluate the filtered MF ROM, their high-fidelity solutions could only serve for validation and not help in constructing the interpolant for the coefficients, since they are not part of the ancestry of the sparse grid. In the 2D diffusion case, this led to the premature termination of the algorithm. The number of consequent important points was not enough to ensure an accurate ROM over the entire phase space. Dynamics were missed which led to errors above the set tolerance of 10^{-3} . Figure 4.9 shows that the FB-POD algorithm samples fewer points in the macroscopic capture cross-section and diffusion coefficient of Region 1 as the algorithm is terminated before the deepest level of important points is reached. The macroscopic fission cross-section already converged with fewer points at a lower level in the grid, and was therefore not affected by the premature termination.

The problem of premature termination could be avoided by dismissing the accuracy check after each iteration. This way, all important points will be utilized in building the MF ROM. Since the low- and high-fidelity models required a comparable amount of important points, it is expected that the accuracy of the filtered MF ROM will improve in this case. The increase in accuracy comes however at the cost of more high-fidelity evaluations. Another solution would be to test the filtered MF ROM after each iteration with one large test set. Since the constructed filtered MF ROM will be tested on a large test set anyways, this same set can be used after each iteration without additional high-fidelity evaluations. This can mitigate the issue of premature termination.

Nonetheless, the majority of the tested points (98.9-99.5%) in the 2D diffusion test case fell under the pre-set global error tolerance. The highest relative error observed was $1.20 \cdot 10^{-3}$ and $1.08 \cdot 10^{-3}$ in the non-greedy and greedy test cases, respectively. The FB-POD method proved itself to effectively reduce the number of high-fidelity solutions while being able to produce accurate approximations when compared to the high-fidelity solution, in the case of multi-grid variable fidelity. In these test cases, the low- and high-fidelity models were still very similar and contained the same dynamics.

In other test cases using variable discretization, problems may occur if the low-fidelity model's discretization becomes too coarse to capture certain behavior accurately. For example, when the mesh size in the 2D neutron diffusion model exceeds the mean free path of neutrons and interactions of neutrons with other particles are missed. If the coarse grid has an insufficient mesh size, the low-fidelity method will likely identify fewer or different points as important. Consequently, the dynamics that arise from the finer mesh of the high-fidelity model will not be accurately represented, as seen in the multi-physics test case. Therefore, mesh convergence tests must be performed on both the low-and high-fidelity models to ensure that they contain sufficient information about the system in their approximations.

In the test case involving multiple physics, the limitations of the FB-POD algorithm became clear. The high-fidelity model incorporated a sine function representing an additional physical phenomenon. The FB-POD algorithm utilized the low-fidelity model, which is a parabolic function dependent solely on parameter A. The root node and the two forward points were deemed important. As the low-fidelity model has a linear dependence on parameter A, the relationship can be approximated using a linear function, which is the interpolant $A_{l,d}$ when 3 supporting nodes are employed. This is illustrated in

Figure 2.1 of Section 2.1.2. However, a filtered MF ROM build on three high-fidelity snapshots does not give accurate approximations, as 99.8% of the 1000 test points exceeded the predefined global threshold of $\gamma_{int}=10^{-3}$. The limitations of the FB-POD algorithm can be explained by the fact that the low- and high-fidelity models include different parameters. The low-fidelity model does not depend on parameters B and C. The adaptive sparse grid search therefore will only sample the first two forward points along those dimensions and will not deem them as important, as these parameters do not affect the system. When transferring these sampled points to the high-fidelity model, the dynamics that parameter B and C introduce is missed by the ROM. Setting the greediness factor to 1 yielded more sampled points but found the same three points important as in the non-greedy case. A greedy FB-POD algorithm does not result in a more accurate filtered MF ROM. It can be concluded that the FB-POD algorithm only works in cases where the models of both fidelity depend on the same parameters.

5.2. Adapted Bi-Fidelity Proper Orthogonal Decomposition

In this study, the AB-POD algorithm was also demonstrated on 1D analytical functions for multi-grid and multi-physics variable fidelity, and on a 2D diffusion model. For the 1D analytical multi-grid case, the number of high-fidelity solutions was reduced by 82-86% depending on the greediness factor. In the 2D diffusion test case with variable discretization, the number of the high-fidelity solution was reduced by 47% in the non-greedy case and 54% in the greedy setting. For both cases, the accuracy of the adapted MF ROM was comparable to that of the high-fidelity aPOD ROM when tested on 1000 test points. Furthermore, utilizing a greedy algorithm did not significantly improve the accuracy of the ROM in both test cases.

The reduction in high-fidelity evaluations can be explained by the similarities between the low- and high-fidelity model. As a result of using a multi-grid variable fidelity approach, the low- and high-fidelity models exhibit similar behavior and handle parameters in the same manner. As the parameters are perturbed, both the low- and high-fidelity models undergo similar changes, such as a steeper parabola or a shifted sinusoidal curve in the 1D analytical case, or an increase in flux density in the 2D diffusion case. However, the difference between the two models changes less significantly, resulting in a smaller impact on the snapshots of the correction factor. This reduced variability between snapshots may explain why only 9 POD modes are needed to approximate the correction factor instead of 13. Because the snapshots are similar, fewer dynamics are found by the ROM and the solution can be approximated with fewer POD modes. A similar result was found in the 2D diffusion case, where only 3 POD modes were used to approximate the correction. The single high-fidelity ROM needed 5 POD modes to approximate the solution in the non-greedy case and 7 in the greedy case. Since a smoother behavior is presumed for each of the coefficients $c_i(\mathbf{p})$ associated with the POD, fewer important points are required to construct the correction factor than in the high-fidelity model. Moreover, in the 1D analytical case, the low-fidelity model's spatial grid points are included in the high-fidelity model, and since they use the same function to calculate values at those points, their solutions are identical. The correction factor remains constantly zero at these points and will not contribute to the approximation error of the adapted MF ROM.

In the multi-physics test case, more training samples are needed for the ROM to approximate the correction factor, which is a sinusoidal function, than the high-fidelity model which is a parabola with a smaller sinusoidal component. An increase of 611-669% in high-fidelity solutions was seen when the AB-POD algorithm was applied over the aPOD algorithm. The lower number of evaluations of the HF ROM can be explained by the fact that the high-fidelity model is mostly a parabola and linearly dependent on parameter A. Figure 4.6a shows that the first squared singular value of the HF ROM is 10^4 times larger than the second largest value. The singular values squared are a measure of the energy contributed by each POD mode to the system. The first POD mode, which corresponds to the parabolic component of the high-fidelity function, captures therefore most of the energy. The POD modes used by the HF ROM are shown in Figure 4.6b. Since the parabola is the dominant feature of the high-fidelity solution and the sinusoidal component constitutes only a fraction of the overall solution, perturbations of parameters B and C will have a lesser impact on the overall solution. As a result, the model's dependent

48 5. Discussion

dence on these parameters can be approximated with lower accuracy while still maintaining a global error below the threshold. Consequently, fewer samples will be required along the dimensions of B and C.

The correction factor, however, is a sinusoidal function. Figure 4.7b displays the POD modes used for approximating the correction factor. It is apparent that the parabolic corresponding mode is absent as it is not needed for approximating a sine function. In Figure 4.7a the squares of the corresponding singular values are given. The first five values are of the same order or magnitude. The interpolants that approximate the corresponding coefficients for these POD modes have to be of comparable accuracy, since these modes contribute similar amounts of energy to the system. Although the correction scales linearly with B and the interpolant requires three supporting nodes to reconstruct the dependency, a large number of samples are required to approximate the highly non-linear frequency parameter C. Specifically, 513 unique values were sampled along the dimension of parameter C to reconstruct the correction factor with a relative error tolerance of $\lambda_{max} = 10^{-3}$.

The results of Section 4.1.2 give insight into overcoming hard-to-learn correction factors by adjusting the global relative error tolerance of approximating the true correction factor. When the relative error tolerance for the correction factor is reduced to 10^{-1} results in 71 high-fidelity evaluations, which is a reduction of 51% in high-fidelity evaluations compared to the HF ROM. When tested on 1000 randomly sampled points, 98.8% of the test points fell below the set global error limit and resulted in a maximum relative error of $1.24 \cdot 10^{-3}$. Since the sinusoidal component accounts for only a portion of the overall solution, it can be approximated with less precision while still maintaining the accuracy of the overall solution. Similar results were obtained in the 2D neutron diffusion test case. The global relative error threshold was set to $\lambda_{max} = 10^{-2}$, while the overall relative error tolerance was set to $\gamma_{max} = 10^{-3}$. Even though the correction factor was less accurately approximated, the adapted MF ROM produced approximations with comparable accuracy to that of the single-fidelity aPOD ROM. By adjusting the global and local error tolerances of the correction factor, a desired balance between the number of high-fidelity evaluations and accuracy can be achieved. Therefore, the AB-POD method offers a flexible trade-off between these two factors and could be a useful tool for many query applications, like design optimization, where not all features have to be approximated with similar accuracy. The balance between accuracy and required computational power can be customized per test case.

Looking into the methods of the neutron diffusion case, the neutron flux is approximated by the adapted MF ROM using 7 POD modes, while the HF ROM and the LF ROM only use 5 in the non-greedy setting. Some extra dynamics are added to the system when corrected low-fidelity snapshots are used instead of pure low- or high-fidelity snapshots. The correction factor that is added is an approximation itself that contains an error. This error might vary from point to point, thereby introducing variation between the snapshots. Moreover, the low-fidelity snapshots are interpolated to match the size of the correction factor, which introduces errors as well. Though Akima interpolation introduces fewer undulations than other methods like spline, the interpolated values will inevitably have so deviations from their highfidelity counterparts. The errors could be recognized by the ROM as system dynamics. Though more POD modes are used to construct the approximation, the maximum relative error of the adapted MF ROM is in the same order of magnitude as the HF-ROM. Figure 4.14 shows that the square singular values of the last two POD modes of the adapted MF ROM have a value in the order of magnitude of 10^{-7} and 10^{-8} , only contributing limited amounts to the overall solution. Furthermore, in Figure 4.9, it can be seen that the AB-POD algorithm samples the same number of unique values per dimension as the high-fidelity model. This indicates that the corrected low-fidelity snapshots contain similar information as the high-fidelity snapshots. To approximate the dependence on each parameter, the same degree of refinement along the dimensions is needed for the adapted MF ROM and HF ROM. The corrected low-fidelity snapshots are constructed such that they mimic the high-fidelity solution. These results indicate that this was successful and that the AB-POD preserves the high-fidelity dynamics through the correction factor.

Furthermore, The global error tolerance to stop iterations for the correction factor was set to $\lambda_{max} = 10^{-2}$, while the global error tolerance that was used for the final multi-fidelity ROM was kept on $\gamma_{max} = 10^{-3}$. Section 3.2.1 revealed that a less accurate approximation to the correction factor still yields an

accurate final multi-fidelity ROM with a lower cost of high-fidelity snapshots. Consequently, the threshold λ_{int} was reduced and resulted indeed in a reduction of high-fidelity snapshots.

5.3. Concluding Remarks

The FB-POD and AB-POD methods were not successfully tested on the third test case due to technical difficulties and time constraints and were produced unreliably. The main problem was the termination of the computation before the ROM had converged. The reason for the early termination was not clear. Moreover, due to long computation times, the termination became apparent late in the process. Because the data was not saved after each iteration, the ROM had to be started all over again. It was attempted to reload sampled solutions into the adaptive grid search, but an insufficient data management strategy prohibited this. It is highly recommended to change the data saving structure of the proposed algorithm, so that data can be stored in between runs, and can be reloaded when premature termination occurs. This will reduce some of the computation time for constructing the ROM. Also, looser error tolerances can be used to limit the number of high-fidelity evaluations. This way, the ROM might converge before the algorithm is prematurely terminated.

This concludes the discussion of the results for the Filtered and Adapted Bi-Fidelity Proper Orthogonal Decomposition. In the following section, the conclusion that can be drawn from the results will be presented along with an outlook for further research.



Conclusions and Recommendations

In this section, the conclusions that can be drawn from the results will be presented. Recommendations for improvements of the presented Filtered- and Adapted Bi-Fidelity Proper Orthogonal Decomposition methods, and for future research will also be given.

The aim of this study was to minimize the computational workload involved in constructing a reduced order model during the offline phase using adaptive sparse grids and multi-fidelity strategies. This was achieved through two novel approaches; the Filtered Bi-Fidelity Adaptive Proper Orthogonal Decomposition and Adapted Bi-Fidelity Adaptive Proper Orthogonal Decomposition. Both methods were evaluated on two different test cases, and the balance between the accuracy of each multi-fidelity ROM and the computational cost, measured by the number of high-fidelity evaluations, was investigated.

6.1. Filtered Bi-Fidelity Proper Orthogonal Decomposition

This study presented a novel approach to filtered bi-fidelity reduced order modeling using Proper Orthogonal Decomposition and adaptive sparse grids. The Filtered Bi-Fidelity Proper Orthogonal Decomposition was tested in three different cases, to assess the computational burden of constructing the filtered multi-fidelity ROM and its performance in terms of accuracy. The success of the proposed method was shown to depend on the specific case, highlighting the reduction of high-fidelity samples in the greedy 1D analytical and 2D diffusion case by 56% and 62% respectively. The results also showed that the number of high- and low-fidelity samples did not need to be set beforehand, as it is determined during the offline phase by the adaptive grid search. The greediness factor was found to be a determining factor in the reduction of high-fidelity samples due to unnecessary refinement along certain directions in the greedy case. Furthermore, it was observed that models of different fidelities should depend on the same parameters in similar ways for the successful construction of the filtered MF ROM. Finally, the accuracy of the filtered MF ROM based on the FB-POD approach was comparable to aPOD reduced order modeling technique in variable discretization cases, demonstrating the potential of this filtered multi-fidelity approach for modeling complex systems.

6.2. Adapted Bi-Fidelity Proper Orthogonal Decomposition

In this thesis, a novel approach to multi-fidelity reduced order modeling using adaptation, POD, and sparse grids is presented. An adapted bi-fidelity reduced order model was constructed and tested in three different test cases. The results showed that the success of the adapted bi-fidelity model is case specific as well, with a reduction of 47-86% of high-fidelity samples in cases based on variable discretization, while maintaining a comparable accuracy to the high-fidelity ROM. A prerequisite for success is that the correction factor needs to be smoother than the high-fidelity model solution, which is not always known beforehand. Additionally, it was demonstrated that the adapted bi-fidelity reduced order model provides flexibility in the trade-off between accuracy and computational power, as the error tolerance of the correction factor can be set independently of the global error tolerances. Notably, it was not required to set the number of high- and low-fidelity samples beforehand, as this is determined during the offline phase by the adaptive grid search. Finally, it was demonstrated that the accuracy of

Adapted Bi-Fidelity model was comparable to that of the aPOD method. These findings contribute to the development of more efficient and accurate reduced order modeling techniques that can be used in a variety of applications.

6.3. Recommendations

Improvements can be made to the FB-POD algorithm in terms of point selection and the interaction between low- and high-fidelity models. The algorithm is now divided into two distinct phases: a preselection of parameter points in the low-fidelity model and a sequential construction of the ROM using the high-fidelity model. These two phases can be more integrated by evaluating important points in high-fidelity after each iteration selecting important points. If the high-fidelity ROM converges before the adaptive grid-search is finished in low-fidelity, then a number of low-fidelity evaluations can be spared. Additionally, the compatibility of the FB-POD algorithm with the test case becomes apparent earlier in the process. If providing more important points to the high-fidelity model does not result in more accurate approximations, it could indicate that the low-fidelity model is searching in the wrong direction. This work found that the FB-POD method was most limited in situations where the high-fidelity and low-fidelity models relied on different parameters. To overcome this issue, a potential solution is to combine various low-fidelity models that capture different dynamics in the system to create a combined set of important points.

To limit the number of high-fidelity evaluations by FB-POD algorithm, the filtered MF ROM was tested after each level of important points was fed. The test points were the important points of the next level. In the 2D diffusion case, however, this led to the premature termination of the algorithm. The number of consequent important points was not enough to ensure an accurate ROM over the entire phase space. This problem could be avoided by dismissing the accuracy check after each iteration. This way, all important points will be utilized in building the MF ROM. Since the low- and high-fidelity models required a comparable amount of important points, it is expected that the accuracy of the filtered MF ROM will improve in this case. The increase in accuracy comes however at the cost of more high-fidelity evaluations. Another solution would be to test the filtered MF ROM after each iteration with one large test set. Since the constructed filtered MF ROM will be tested on a large test set anyways, this same set can be used after each iteration without additional high-fidelity evaluations. This can mitigate the issue of premature termination.

Other filtering criteria can be explored as well. The main criterion of deeming points as important is based on the error between the true solution and the ROM approximation in the l_2 norm. If certain areas of the system are of particular interest, the adaptive grid search can be directed toward those directions. Important points would then be selected based on if the ROM can approximate the solution accurately enough in only certain parts of the system. The ROM can also become more goal-oriented by refining the accuracy of a response derived from the solution, like a detector response, instead of the solution itself.

Furthermore, improvements can be made to the AB-POD algorithm. The method is most limited in cases where the dependence of the parameters on the correction factor is more difficult to learn than the high-fidelity solution itself. It was shown that the correction factor does not have to be approximate with the same level of accuracy as the high-fidelity solution. More research with different error tolerance can be done to investigate the influence of poorly approximated correction factors on the solution produced by the adapted MF ROM. As lower error tolerances for the correction factor reduce the number of high-fidelity evaluations, finding limits for the error tolerances could lead to a further decrease in high-fidelity evaluations during the construction of the adapted MF ROM. Furthermore, constructing the correction factor using a ROM can be computationally intensive. As this research has shown, when models of high- and low-fidelity are similar, the correction factor does not have to be as accurately approximated. Simpler interpolation schemes for the correction factor can be tested to lift some of the computational load of the offline phase of reduced order modeling.

In this study, due to technical difficulties and time constraints, the proposed multi-fidelity methods were

6.3. Recommendations 53

not properly tested for solving the Neutron Transport Equation using Phantom-DG. As this test case relies on a different form of variable fidelity, different angular discretizations, it can present itself as an interesting test case. It is expected that the filtering method will perform best in the thick material test case, as a coarser angular discretization will have less effect on the neutron flux. This is assumed because more scattering of the neutrons will occur in the thick material, thereby scattering them more isotropically away from the source. As the low- and high-fidelity solutions will be similar, FB-POD is assumed to select the right points in low-fidelity, and enough information is transferred to the high-fidelity part. The AB-POD is also assumed to perform well in thick material due to the similar nature of the low-and high-fidelity solutions. The responses of both models to perturbations in parameters are assumed to be similar, thereby creating a smooth correction field between the two. In the thin material, rays effects are expected in the low-fidelity solution. It will be interesting to investigate how these unnatural effects will be handled by FB-POD and AB-POD methods.

In this work, two out of the three multi-fidelity strategies were applied and tested. The multi-fidelity through fusion scheme can be explored. The manifold alignment technique of Perron et al.(2022) based on Proper Orthogonal Decomposition can conveniently be linked to the aPOD framework due to the similar underlying mathematical framework [9]. Also, the employment of neural networks and manifold alignment in multi-fidelity methods are both still quite novel and could be an interesting path to explore.

Lastly, though these multi-fidelity non-intrusive reduced-order models were used to analyze the behavior of nuclear reactors, they can be applied in any other field of science and engineering due to the non-intrusive nature of the reduced-order modeling technique.

Bibliography

- [1] Hiroshi Akima. "A New Method of Interpolation and Smooth Curve Fitting Based on Local Procedures". In: *J. ACM* 17.4 (Oct. 1970), pp. 589–602. ISSN: 0004-5411. DOI: 10.1145/321607. 321609. URL: https://doi.org/10.1145/321607.321609.
- [2] Fahad Alsayyari. "Adaptive Data-Driven Reduced Order-Modelling Techniques for Nuclear Analysis". PhD thesis. Delft University of Technology, Oct. 2020.
- [3] Fahad Alsayyari et al. "Analysis of the Molten Salt Fast Reactor using reduced-order models". In: Progress in Nuclear Energy 140 (2021), p. 103909. ISSN: 0149-1970. DOI: https://doi.org/10.1016/j.pnucene.2021.103909. URL: https://www.sciencedirect.com/science/article/pii/S0149197021002729.
- [4] M. Gunzburger B. Peherstorfer K. Willcox. "Survey of Multifidelity Methods in Uncertainty Propagation, Inference, and Optimization". In: *SIAM REVIEW* 60 (3 2018), pp. 550–591. DOI: 10. 1137/16M1082469.
- [5] Y. Marzouk K. Willcox B. Peherstorfer T. Cui. "Multifidelity importance sampling". In: Computer Methods in Applied Mechanics and Engineering 300 (2016), pp. 490–590. ISSN: 0045-7825. DOI: https://doi.org/10.1016/j.cma.2015.12.002. URL: https://www.sciencedirect.com/science/article/pii/S0021999115003654.
- [6] Peter Benner, Serkan Gugercin, and Karen Willcox. "A Survey of Projection-Based Model Reduction Methods for Parametric Dynamical Systems". In: SIAM Review 57 (June 2015), pp. 483–531. DOI: 10.1137/130932715.
- [7] Martin Gariépy Benoit Malouin Jean-Yves Trépanier. "Interpolation of Transonic Flows Using a Proper Orthogonal Decomposition Method". In: *International Journal of Aerospace Engineering* 2013 (2013). DOI: 10.1155/2013/928904. URL: https://doi.org/10.1155/2013/928904.
- [8] Vladimir Buljak. "Proper Orthogonal Decomposition and Radial Basis Functions for Fast Simulations". In: Inverse Analyses with Model Reduction: Proper Orthogonal Decomposition in Structural Mechanics. Berlin, Heidelberg: Springer Berlin Heidelberg, 2012, pp. 85–139. ISBN: 978-3-642-22703-5. DOI: 10.1007/978-3-642-22703-5_3. URL: https://doi.org/10.1007/978-3-642-22703-5_3.
- [9] D. Rajaram Corman J. C. Perron D. Sarojini and D. Mavris. *Manifold Alignment-Based Multi-Fidelity Reduced-Order Modeling Applied to Structural Analysis*. **2022**. DOI: 10.48550/ARXIV. 2206.06920. URL: https://arxiv.org/abs/2206.06920.
- [10] Huachao Dong et al. "Multi-fidelity information fusion based on prediction of kriging". In: *Structural and Multidisciplinary Optimization* 51 (Dec. 2014). DOI: 10.1007/s00158-014-1213-9.
- [11] Michael Eldred, A Giunta, and Samuel Collis. "Second-Order Corrections for Surrogate-Based Optimization with Model Hierarchies". In: (Aug. 2004). DOI: 10.2514/6.2004-4457.
- [12] Danny Lathouwers Fahad Alsayyari Zoltan Perko and Jan Leen Kloosterman. "A nonintrusive reduced order modelling approach using Proper Orthogonal Decomposition and locally adaptive sparse grids". In: *Journal of Computational Physics* 399 (2019), p. 108912. ISSN: 0021-9991. DOI: https://doi.org/10.1016/j.jcp.2019.108912. URL: https://www.sciencedirect.com/science/article/pii/S0021999119306175.
- [13] Generation IV International Forum. Annual Report 2020. 2020.
- [14] Z. Gajic. *Linear Dynamic Systems and Signals*. Prentice Hall/Pearson Education, 2003. ISBN: 9780201618549. URL: https://books.google.nl/books?id=yOhiQgAACAAJ.

56 Bibliography

[15] Shawn E. Gano, John E. Renaud, and Brian Sanders. "Hybrid Variable Fidelity Optimization by Using a Kriging-Based Scaling Function". In: *AIAA Journal* 43.11 (2005), pp. 2422–2433. DOI: 10.2514/1.12466. eprint: https://doi.org/10.2514/1.12466. URL: https://doi.org/10.2514/1.12466.

- [16] Charles F. Van Loan Gene H. Golub. "Matrix Computations, Fourth Edition". In: Berlin, Heidelberg: The Johns Hopkins University Press, 2013, pp. 76–81. ISBN: 9781421408590.
- [17] Richard Haberman. *Applied Partial Differential Equations*. Pearson, 2013, p. 1. ISBN: 9780321797056. URL: https://www.worldcat.org/nl/title/applied-partial-differential-equations-with-fourier-series-and-boundary-value-problems/oclc/793099447.
- [18] Philip Holmes et al. *Turbulence, Coherent Structures, Dynamical Systems and Symmetry.* 2nd ed. Cambridge Monographs on Mechanics. Cambridge University Press, 2012. DOI: 10.1017/CB09780511919701.
- [19] Louis J. Hamilton James J. Duderstadt. *Nuclear Reactor Analysis*. John Wiley Sons, 1976. ISBN: 0-471-222363-8.
- [20] Stanley Z Jerrold F. "Curve fitting by spline and akima methods: possibility of interpolation error and its suppression." In: *Physics in Medicine and Biology* 18.4 (1973), pp. 550–558. DOI: 10. 1088/0031-9155/18/4/306. URL: https://doi.org/10.1088/0031-9155/18/4/306.
- [21] M. C. Kennedy and A. O'Hagan. "Predicting the Output from a Complex Computer Code When Fast Approximations Are Available". In: *Biometrika* 87.1 (2000), pp. 1–13. ISSN: 00063444. URL: http://www.jstor.org/stable/2673557.
- [22] Jozsef Kophazi and Danny Lathouwers. "A space-angle DGFEM approach for the Boltzmann radiation transport equation with local angular refinement". In: Journal of Computational Physics 297 (2015), pp. 637–668. ISSN: 0021-9991. DOI: https://doi.org/10.1016/j.jcp. 2015.05.031. URL: https://www.sciencedirect.com/science/article/pii/s0021999115003654.
- [23] Dehao Liu and Yan Wang. "Multi-Fidelity Physics-Constrained Neural Network and Its Application in Materials Modeling". In: *Journal of Mechanical Design* 141.12 (Sept. 2019). 121403. ISSN: 1050-0472. DOI: 10.1115/1.4044400. eprint: https://asmedigitalcollection.asme.org/mechanicaldesign/article-pdf/141/12/121403/5873989/md_141_12\ 121403.pdf. URL: https://doi.org/10.1115/1.4044400.
- [24] Hung V. Ly and Hien T. Tran. "Modeling and control of physical processes using proper orthogonal decomposition". In: *Mathematical and Computer Modelling* 33.1 (2001). Computation and control VI proceedings of the sixth Bozeman conference, pp. 223–236. ISSN: 0895-7177. DOI: https://doi.org/10.1016/S0895-7177 (00) 00240-5. URL: https://www.sciencedirect.com/science/article/pii/S0895717700002405.
- [25] Yongtao Lyu. Finite element method: element solutions. Springer, 2022. DOI: 10.1007/978-981-19-3363-9. URL: https://doi.org/10.1007/978-981-19-3363-9.
- [26] R. Masson M.R. Tonks R. Williamson. *Finite element modelling*. International Atomic Energy Agency, 2015. Chap. 22. URL: https://inis.iaea.org/collection/NCLCollectionStore/Public/47/032/47032428.pdf.
- [27] Richard Martin. Meltdown-Proof Nuclear Reactors Get a Safety Check in Europe. URL: https://www.technologyreview.com/2015/09/04/166330/meltdown-proof-nuclear-reactors-get-a-safety-check-in-europe. (accessed: 24.02.2022).
- [28] MATLAB. *Interp2 (R2021a)*. Retrieved January 28, 2023: The MathWorks Inc., 2023. URL: https://nl.mathworks.com/help/matlab/ref/interp2.html.
- [29] Schoefs F. Mell L Rey V. "Multifidelity adaptive kriging metamodel based on discretization error bounds." In: *International journal for numerical methods in engineering*. 20 (121 2020), pp. 4566–83. DOI: 10.1002/nme.6451. URL: https://doi.org/10.1002/nme.6451..

Bibliography 57

[30] Xuhui Meng and George Em Karniadakis. "A composite neural network that learns from multifidelity data: Application to function approximation and inverse PDE problems". In: *Journal of Computational Physics* 401 (2020), p. 109020. ISSN: 0021-9991. DOI: https://doi.org/10.1016/j.jcp.2019.109020. URL: https://www.sciencedirect.com/science/article/pii/S0021999119307260.

- [31] Thomas P. Prescott and Ruth E. Baker. "Multifidelity Approximate Bayesian Computation". In: SIAM/ASA Journal on Uncertainty Quantification 8.1 (2020), pp. 114–138. DOI: 10.1137/18M1229742. URL: https://doi.org/10.1137/18M1229742.
- [32] Fabian Albert Braeu Roland Can Aydin and Christian Johannes Cyron. "General Multi-Fidelity Framework for Training Artificial Neural Networks with Computational Models". In: Frontiers in Materials 6 (2019). DOI: 10.3389/fmats.2019.00061. URL: https://www.frontiersin.org/articles/10.3389/fmats.2019.00061/full.
- [33] J. Rommes W.H.A. Schilders H.A. van der Vorst. *Model Order Reduction:Theory, Research Aspects and Applications*. Springer, 2008, pp. 3–8.
- [34] D. Xiao et al. "Non-intrusive reduced-order modelling of the Navierâ€"Stokes equations based on RBF interpolation". In: *International Journal for Numerical Methods in Fluids* 79.11 (2015), pp. 580–595. DOI: https://doi.org/10.1002/fld.4066. eprint: https://onlinelibrary.wiley.com/doi/pdf/10.1002/fld.4066. URL: https://onlinelibrary.wiley.com/doi/abs/10.1002/fld.4066.
- [35] M. Breitkopf P. Filomeno Coelho R. et al. Xiao. "Model reduction by CPOD and Kriging." In: Structural and Multidisciplinary Optimization 41.4 (2010), pp. 555–574. DOI: 10.1007/s00158-009-0434-9. URL: https://doi.org/10.1007/s00158-009-0434-9.
- [36] Xinshuai Zhang et al. "Multi-fidelity deep neural network surrogate model for aerodynamic shape optimization". In: Computer Methods in Applied Mechanics and Engineering 373 (2021), p. 113485. ISSN: 0045-7825. DOI: https://doi.org/10.1016/j.cma.2020.113485. URL: https://www.sciencedirect.com/science/article/pii/S0045782520306708.